Global and Planetary Change 195 (2020) 103322

Contents lists available at ScienceDirect

Global and Planetary Change

journal homepage: www.elsevier.com/locate/gloplacha

Strength variations of the Australian continent: Effects of temperature, strain rate, and rheological changes

Magdala Tesauro[a,b,*], Mikhail K. Kaban[c,d], Alexey G. Petrunin[c,d], Alan R.A. Aitken[e]

[a] Dipartimento di Matematica e Geoscienze, Università di Trieste, Italy
[b] Department of Earth Sciences, Utrecht University, the Netherlands
[c] GFZ German Research Centre for Geosciences Potsdam, Germany
[d] Schmidt Institute of Physics of the Earth, Moscow, Russia
[e] School of Earth Sciences, The University of Western Australia, Australia

ARTICLE INFO

Keywords:
Australian Lithosphere
Thermal Model
Crustal Rheology
Strength Model
Effective Elastic Thickness

ABSTRACT

The Australian continent is composed of several geologic provinces, showing a general age progression from Archean in the west to Phanerozoic in the east. The lithospheric heterogeneity and complex tectonic history of this region make it a key area for studying the thermal and rheological structure of the geological provinces and testing the influence of different conditions, such as temperature, rheology, and strain rate on the plate strength. In a previous study, temperature and compositional variations of the Australian upper mantle have been determined based on a joint interpretation of the seismic tomography and gravity data. In this study, we further implement a thermal model of the crust, based on available surface heat flow data from regional and global database. The crustal and upper mantle thermal models show different anomalies distribution, indicating a significant variation of the thermal conditions with depth. The new thermal models are used to estimate strength and effective elastic thickness (*Te*) distribution in the lithosphere. For this aim, we assigned the rheology of the crust based on the seismic velocities provided by the AuSREM model and used the strain rate values obtained from a global mantle flow model, constrained by seismic and gravity data. The maximal strength and *Te* are found in the West Australian Craton, on account of the low temperatures in the lithospheric mantle. We found that locations of the intraplate earthquakes attend to sharp changes in the lithospheric strength. Comparison of the results with those obtained for uniform rheology and strain rate, indicate that in the Officer basin the variations of the crustal rheology enhance the effect of temperature changes, while in the Yilgarn craton they reduce it. On the other hand, the lower values of the strain rate in the cratons than in the Phanerozoic regions influence the strength/*Te* in the opposite way with respect to temperatures.

1. Introduction

Knowledge of the thermal and compositional structure of the Earth's lithosphere is crucial for understanding of the geodynamic processes that determine its evolution, both at a regional and global scale. Both variations in temperature and composition control lithospheric rheological behavior, which has a direct influence on the long-term stability of tectonic structures, as well as on the deformation along plates margins and mechanical stress distribution. Temperature variations within the lithosphere control the depth of the brittle-to-ductile transition (e.g., Goetze and Evans, 1979), and thus have a direct influence on earthquakes nucleation. High temperatures trigger the plastic behavior of the lithosphere and lower crustal flow, which in turn can cause lithospheric instabilities and promote exhumation and delamination processes (e.g., Burov, 2011; Tesauro et al., 2011). On the other hand, compositional variations influence the distribution of the heat-producing elements (HPEs), directly affecting the thermal state of the lithosphere, as well as rheological properties. Furthermore, both temperature and composition are responsible for the density variations in the crust and upper mantle, which cause isostatic adjustments (i.e., uplift and subsidence) on a regional scale.

Variations of the thermal and rheological parameters of the lithosphere have been investigated using xenolith and surface heat flow (*HF*) measurements (e.g., Lee, 2003; Lucazeau, 2019) and indirect methods (e.g., Watts and Burov, 2003; Tesauro et al., 2012). Studies on a regional scale make it possible to analyze the thermophysical structure of the geological provinces and make comparisons between them. In this way, it is possible to relate the results obtained with the history of the

* Corresponding author at: Dipartimento di Matematica e Geoscienze, Università di Trieste, Italy.
E-mail address: mtesauro@units.it (M. Tesauro).

https://doi.org/10.1016/j.gloplacha.2020.103322
Received 20 April 2020; Received in revised form 26 August 2020; Accepted 14 September 2020
Available online 21 September 2020
0921-8181/

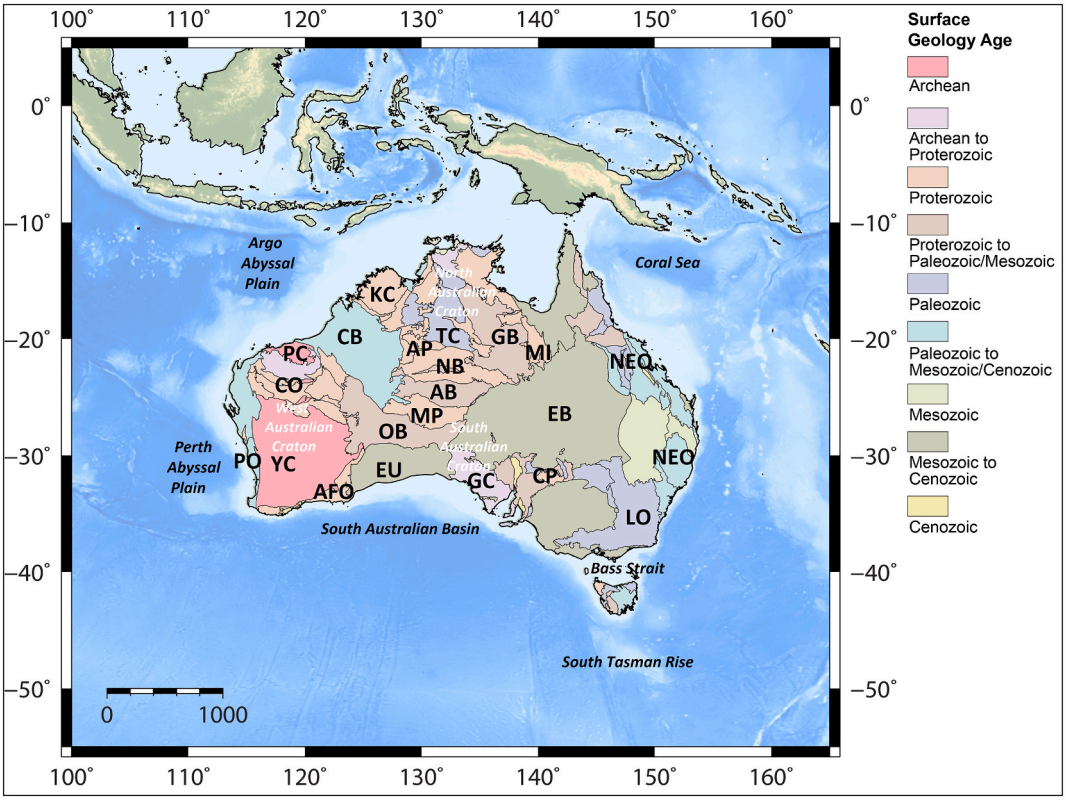

Fig. 1. Age of the crystalline crust of the Australian continent (modified after Aitken et al., 2015). Red labels show the abbreviations of the names of the main tectonic provinces as follows: *West-Australian Craton*: **PC**—Pilbara Craton, **YC**—Yilgarn Craton, **CO**—Capricorn Orogen. *South Australian Craton*: **CP**—Curnamona Province, **GC**—Gawler Craton. *North Australian Craton*: **AP**—Arunta Province, **KC**—Kimberley Craton, **MI**—Mt Isa Inlier. *Proterozoic Orogens*: **AFO**—Albany–Fraser Orogen, **MP**—Musgrave Province; **TC**—Tennant Creek. *Phanerozoic Orogens*: **DO**—Delamerian Orogen, **LO**—Lachlan Orogen, **NEO**—New England Orogen; **NEQ**—North East Queensland; **PO**—Pinjarra Orogen *Major Sedimentary Basins*: **EU**—Eucla Basin, **OB**—Officer Basin, **AB**—Amadeus Basin, **CB**—Canning Basin, **NB**—Ngalia Basin, **GB**—Georgina Basin, **EB**—Eromanga Basin. *Phanerozoic volcanism*: **NVP**—Newer Volcanics Province. (For interpretation of the references to colour in this figure legend, the reader is referred to the web version of this article.)

tectonic features and predict their evolution (e.g., Burov, 2011). For this reason, we chose the Australian continent as a study area, which is composed of geological provinces having different ages and tectonic history (Fig. 1). Precambrian Australia is made up of three Archean cratons: the West, North, and South Australian cratons (WAC, NAC, and SAC, respectively), which are separated by Proterozoic orogenic belts and/or Phanerozoic sedimentary basins. The Phanerozoic Tasmanides in the east of Australia were accreted onto the eastern margin of the Precambrian craton in the late Paleozoic in a series of stages. The crust and upper mantle structure of Australia has been deeply investigated in the last two decades using a variety of geophysical methods, among the others, seismic tomography (e.g., Fishwick and Reading, 2008; Fichtner et al., 2010; Kennett et al., 2013; Rawlinson et al., 2014), gravity and magnetic studies (Aitken et al., 2015; Chopping and Kennett, 2015). The thermal structure of the crust and upper mantle has been analyzed through surface *HF* measurements (e.g., Cull, 1982; Siégel et al., 2014) and inversion of seismic tomography (Goes et al., 2005). In the previous study of Tesauro et al. (2020), we applied an iterative technique, which jointly interprets seismic tomography and gravity data, to construct a complete thermal, density, and compositional model of the mantle lithosphere of the Australian plate. However, an integrative study of the crust and upper mantle of the Australian continent, which discuss the thermophysical structure and stability of the tectonic features, is still missing.

Temperature distribution within the lithosphere is usually inferred from heat flow measurements in boreholes, assuming a purely conductive heat transfer mechanism (e.g. Afonso et al., 2013; Békési et al., 2018). Indeed, reconstructions of the thermal transient conditions of the lithosphere require precise knowledge of its past thermal variations, which are often missed. Furthermore, Siégel et al. (2014) demonstrated that the steady-state assumption may be valid and the effects of advective, convective, or transient heat transfer are likely to be minor at the regional scale. For construction of a new thermal model of the crust, we employed the *HF* data recently published in regional and local studies and the crustal seismic velocity provided by the seismic tomography model AuSRem (http://rses.anu.edu.au/seismology/AuSREM/index.php). These data were used to calculate the heat generation and temperature distribution in the crust, assuming steady-state conditions (sections 2.1–2.2). Furthermore, we combine these results with the mantle temperatures distribution, obtained by Tesauro et al. (2020), to construct a complete lithospheric thermal model (section 2.3). We use then the seismic velocities from the AuSREM model to identify different rheological crustal types (section 3.2). The new thermal and rheological model together with the strain rate values, obtained from a global mantle convection model (section 3.3), are used as an input for calculation of the strength (section 3.1 and 3.4) and effective elastic thickness (*Te*) of the lithosphere (sections 4.1–4.3). The obtained results are compared with the distribution of the intraplate seismicity.

The thermal models and other input parameters, as rheology and strain rates, used to calculate strength and *Te* are affected by some uncertainties, that unfortunately remain in general undefined. However, it is possible to identify the general physical characteristics of the geological provinces composing the Australian plate and, by performing additional tests, to discuss the influence of the input parameters on the strength/*Te* and thus, on their long-term tectonic stability.

2. Thermal model of the Australian plate

2.1. Method

We construct a thermal model of the crust, assuming the steady-state conditions and calculating the geotherms with an iterative method (1 and 2). Following the approach of Hasterock and Chapman (2011), we divide the crust into 500 m thick layers, in order to take into account vertical variation of the heat generation and thermal conductivity.

$$T_{i+1} = T_i + \frac{q_i}{\lambda_i}\Delta z_i - \frac{A_i}{2\lambda_i}\Delta z_i^2 \quad (1)$$

and

$$q_{i+1} = q_i - A_i \Delta z_i \quad (2)$$

where the temperature and *HF* values at the bottom of each layer of the thickness Δz_i (T_{i+1}, and q_{i+1}, respectively) are determined from those at the top (T_i, and q_i). The surface *HF* values have been obtained from the observed data available for the Australian continent (section 2.2). The intra-layer heat generation (A_i) is calculated using the empirical relationship with a seismic velocity of Rybach and Buntebarth (1984) for the Proterozoic crust:

$$\ln(A) = B - 2.17V_p \quad (3)$$

where A is the heat generation (μWm^{-3}), Vp is the compressional seismic velocity (km/s), and B is a constant value equal to 12.6. This relationship between the velocity and heat generation is smoother with respect to the other proposed relationships (e.g., Čermák et al., 1990; Cull, 1991) and thus reduces the effect of the velocity uncertainties (Fig. 2). We employ the V_p values provided by the AuSREM model for the depths where the values fall in the range 5.5–8.1 km/s. AuSREM provides *P* wavespeed (and also *S* wavespeed) distributions through the crust (from 5 to 60 km depth, with a step of 5 km) and upper mantle (from 50 to 300 km with a step of 25 km), derived by different methods, among the others, ambient noise tomography for the crust (Kennett et al., 2013; Kennett and Salmon, 2012; Salmon et al., 2013). It is assumed that the surface temperature is equal to 0 °C and that the A_i is equal to the value corresponding to $V_p = 5.5$ km/s at depths where V_p is < 5.5 km/s.

The intra-layer conductivity (λ_i) is calculated depending on the temperature and depth according to Chapman (1986):

$$\lambda(T,z) = \frac{\lambda_0(1+cz)}{(1+bT)} \quad (4)$$

where c and b are the pressure and temperature coefficient, respectively. As in the study of Chapman (1986), for the upper crust b is assumed equal to 1.5×10^{-3} K^{-1}, which is an intermediate value between those ones corresponding to granite and granodiorite, while for the lower crust the value 1.0×10^{-4} is used (Chapman, 1986). The value for the pressure coefficient c is kept constant (1.5×10^{-3} km^{-1}) for the entire crust. λ_o is the conductivity at the ambient temperature and pressure and is assumed equal for both the upper and lower crust (3 Wm^{-1} K^{-1}). This value is in the range of those estimated for different crystalline rocks of the Australian continent (Cull and Conley, 1983).

To apply eq. (4), we divided the whole crust (Fig. 3a), between the top of topography (downscaled *Etopo1*, https://www.ngdc.noaa.gov/mgg/global/) and the Moho provided by the model of Salmon et al. (2013), into the upper and lower layers. For this purpose, we considered that the upper crust thickness is 60% of the entire crustal thickness. This assumption is supported by the crustal models for other continents, such as Europe and North America, in which the predominantly mafic part of the crust, corresponding to the lower crustal layer, is thinner than the sialic (upper) layer (Tesauro et al., 2008; Tesauro et al., 2014).

We preferred not to use the steady-state approach to calculate the temperatures in the upper mantle, since the uncertainties of the geotherm due to those of the crustal thermal parameters increase with depth (Hasterock and Chapman, 2011). Furthermore, the relation of the thermal conductivity, temperature, and pressure becomes more complex and more uncertain in the lithospheric mantle (Hasterock and Chapman, 2011). Finally, recent tectonic activities could initiate thermal transient processes in the upper mantle (e.g., mantle upwelling), which takes time to diffuse to the crust, but makes invalid the extension of the steady-state approach below the Moho depth.

Indirect methods, such as inversion of seismic velocities into temperatures are more suitable to get reliable geotherms in these conditions, since the velocities are directly related to the present-day physical parameters. In the previous study of Tesauro et al. (2020), the temperature distribution in the upper mantle has been estimated by inverting the mantle seismic velocities for temperature, initially using a uniform composition, suitable for a "fertile" upper mantle. This temperature was then iteratively corrected for compositional changes (depletion) in the cratonic areas, according to compositional density

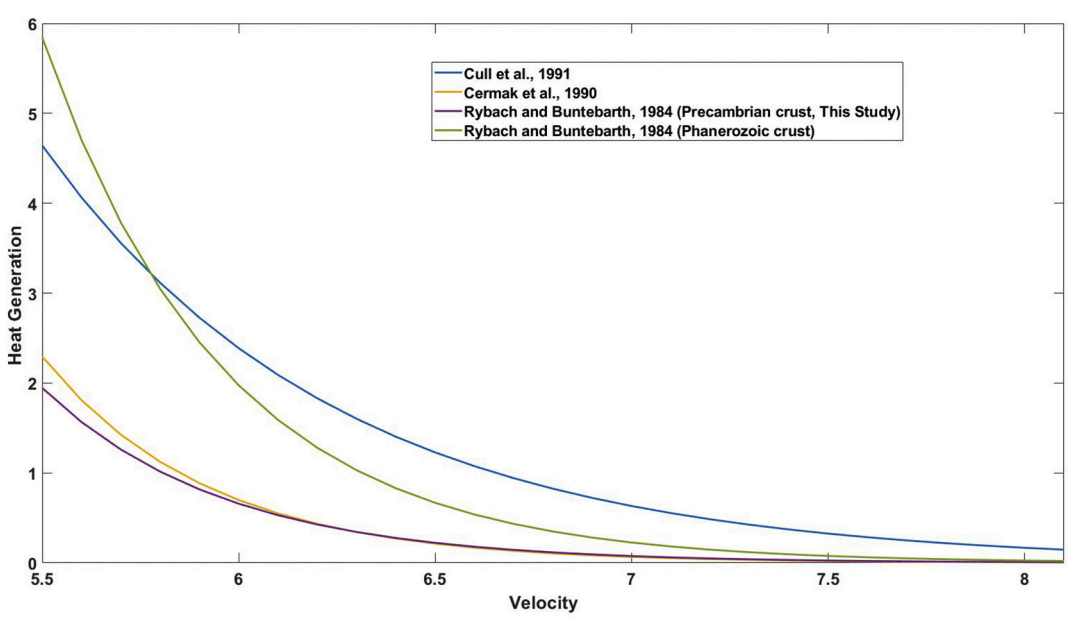

Fig. 2. Empirical relationships between heat generation ($\mu W/m^3$) and seismic velocity (km/s) proposed by different studies.

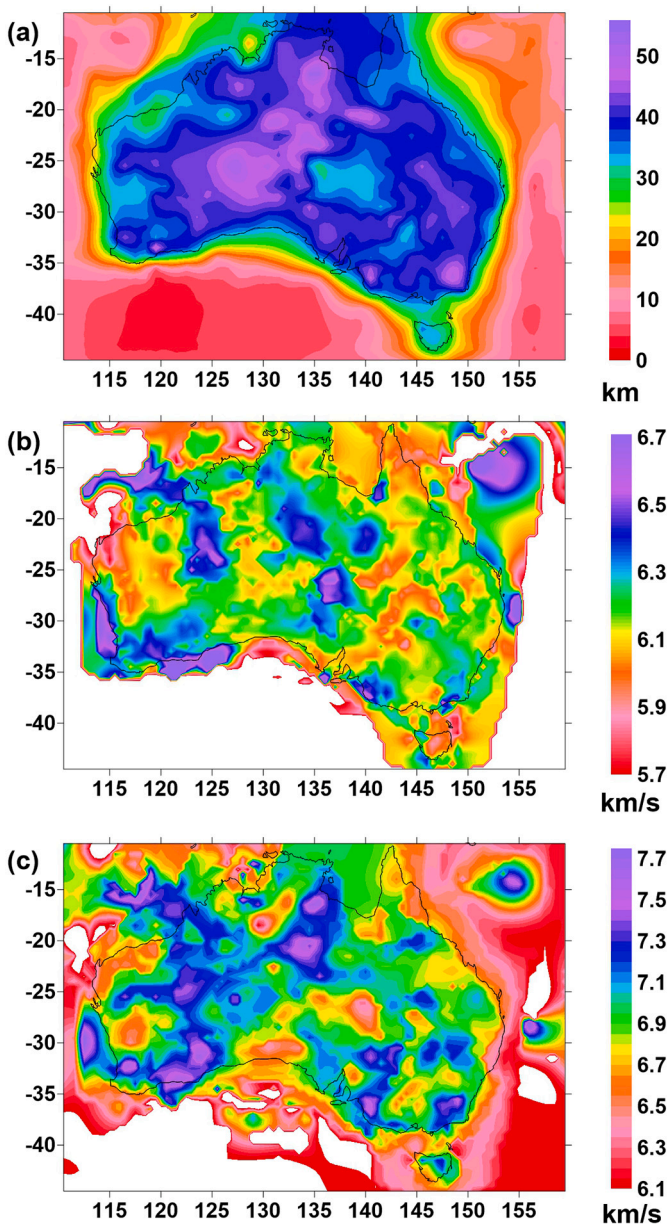

Fig. 3. (a-c) (a) Crustal thickness and **(b)** average crustal velocity (km/s) of the upper crust and **(c)** lower crust. The average values are calculated from the AuSREM model, excluding the values below 5.5 km/s. The blanked off-shore areas are those having the average velocity lower than the minimum value observed in the continental regions (< 5.7 km/s and < 6.1 km/s in the upper and lower crust, respectively). The upper/lower layers division is made considering the thickness of the upper crust equal to 60% of the entire thickness of the crust.

variations obtained from the inversion of the mantle gravity anomalies and residual topography. The upper mantle temperatures obtained by Tesauro et al. (2020) have been combined with those for the crust in a thermal model, leaving a buffer zone between the Moho depth and depth of 100 km, in which the temperatures have been obtained by interpolation of the two models.

2.2. Surface heat flow

We collected more than 1000 surface *HF* data falling in the study area, using regional (Cull, 1982; Mather et al., 2018; McLaren et al., 2003; Matthews and Beardsmore, 2007; Matthews et al., 2013; Goutorbe et al., 2008; Pollett et al., 2019) and global databases (Lucazeau, 2019), Fig. 4. The *HF* values are unevenly distributed within the continental Australia, with higher concentration along its margins and in the tectonically active regions, as the volcanic areas located in the southeastern part of the continent. Some data sets (e.g., Cull, 1982; Lucazeau, 2019) provide a quality analysis of the *HF* data, based on the depth of the measurements and borehole conditions. On the base of this analysis, we excluded from our compilation the values below the assumed quality threshold. We also excluded the values higher than 90 mWm^{-2}, which likely reflect the effect of magmatic intrusion or hydrothermal circulation. The remaining data were interpolated on the 0.5°x0.5° grid, using a standard kriging method (SURFER, Golden Software package) (Fig. 4).

We analyzed the patterns of surface *HF* values together with *P*-wave crustal velocities provided by the AuSREM model, in order to discuss the thermo-compositional structure of the crust. For this purpose, we calculated the average *P*-wave velocities in the upper and lower crust, considering all the values higher than 5.5 km/s provided by the AuSREM model. In the continental areas, the average velocities of the upper crust are between 5.7 km/s and 6.4 km/s, while in the lower crust span over a wider range, between 6.4 and 7.7 km/s (Fig. 3b-c). As stated in the introduction, analysis of our results is mainly qualitative, on account of the uncertainties of data input, leading to identify principal differences between main tectonic structures. In particular, we consider only extended anomalies exceeding a few hundred kilometres, which are constrained by many data points, but not local variations, which might be related to artifacts in the input data. The resulting surface *HF* map shows values between 26 and 89 mWm^{-2} (Fig. 4). In general, large values of the surface *HF* are related to the high concentration of radiogenic elements or are effects of recent volcanism, while the low values reflect the presence of rocks having a more mafic composition (e.g., Cull, 1982; Chopping and Kennett, 2015). We identify areas characterized by low (< 50 mWm^2), moderate (50–70 mWm^2), and high values (> 70 mWm^2), which are divided by boundaries of a few tens of km wide, where the *HF* changes by up to 20%. These sharp variations can only be attributed to shallow heat sources (upper-middle crustal depth).

The *HF* patterns are not strictly related to the crustal age (Fig. 4). Western Australia shows large variability of the surface *HF* values (20–70 mWm^{-2}), although its Archean crystalline crust is expected to be depleted of radiogenic elements. However, this area hosts several large sedimentary basins, including the Perth, Carnarvon, and Canning basin, which are partly underlain by the crystalline rocks with a high concentration of heat-generating elements (Haynes et al., 2015; Middleton, 2016). We can observe a sharp difference between the western part of the Yilgarn and Pilbara craton, characterized by moderate *HF* values, with respect to the eastern part of the WAC, Officer and Eucla basin, where the low *HF* values (< 40 mWm^{-2}) suppose the presence of a more mafic crust. These results are supported by the crustal seismic velocity distribution, showing low average values (5.7–6.2 km/s) in the upper crust beneath the western part of the WAC and the northern part of the Canning basin, indicating a felsic crust enriched with HPEs. On the other hand, the average velocity in the upper crust increases to about 6.2–6.5 km/s beneath the eastern part of the WAC and Canning basin, as well as in the western part of the Eucla and Officer basin, confirming a more mafic composition.

The *HF* data in the central part of Australia show a sharp variation from moderate to high values from north to south across the NAC, Amadeus basin, Musgrave Province, and the SAC. The average values higher than 80 mWm^{-2} are observed near Tennant Creek (20° S, 134°E). This value is much higher than the global average of the *HF* data in the Proterozoic terranes, and it may be caused by high heat production in the crustal rocks (e.g., Cull, 1982; McLaren et al., 2003), or by a mantle source, or, alternatively, represents the transient *HF* related to neotectonic activity (e.g., Fishwick and Reading, 2008). The high velocity in the upper crust (6.45 km/s) suggests a mafic

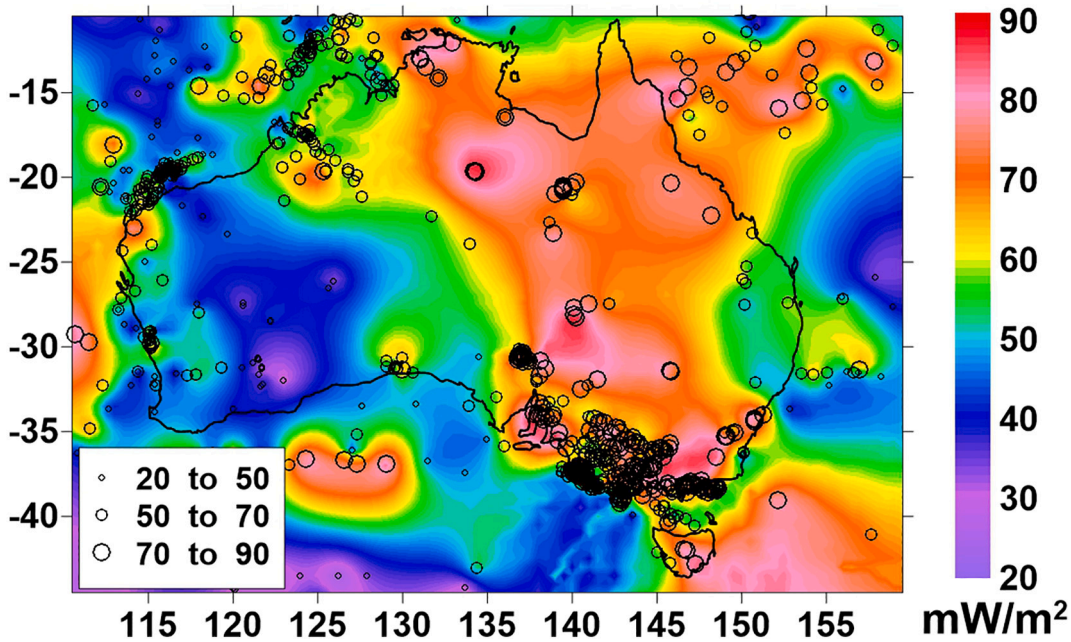

Fig. 4. Surface heat flow map (mWm^{-2}). Black circles show locations of the heat flow measurements used in this study taken from the database of Cull (1982); Mather et al. (2018); McLaren et al. (2003); Matthews and Beardsmore (2007); Matthews et al. (2013); Goutorbe et al. (2008); Lucazeau (2019); Pollett et al. (2019).

composition. Therefore, the large values of the surface *HF* are likely due to a hot mantle or to local outcropping Proterozoic sialic rocks enriched with HPEs (Siégel et al., 2014).

The anomalously high surface *HF* extends south and east of Tennant Creek, including the Georgina basin, Musgrave Inliers, and the Eromanga basin. According to the study of Sandiford et al. (2001), this heat flow anomaly can be related to the high concentration of HPEs (5.9 ± 1.7 Wm^{-3}) in the Mesoproterozoic granitic rocks outcropping in the Arunta and Musgrave Inliers. Most part of the Eromanga basin is characterized by low upper crustal velocities (< 6.0 km/s), which coincide with a large shallow (< 5 km) thermal anomaly and Curie depth (Chopping and Kennett, 2015). The lower crust in the western part of the Eromanga basin can also contribute to the high HF, having low velocities (6.5–6.8 km/s), which suppose a silicic composition (Siégel et al., 2014).

Southward, the sharp transition from moderate to high surface *HF* values crosses the Gawler craton, where we observe changes from 55 mWm^{-2} in the western part to 70 mW m^{-2} in the eastern part, in agreement with previously published heat flow maps (Raimondo et al., 2014). The SW corner of Queensland is also characterized by anomalously elevated *HF* and form the South Australian Heat Flow Anomaly (SAHFA). According to previous studies (e.g., McLaren et al., 2002; Sandiford et al., 2002), these large values of surface *HF* are related to abnormal enrichment of HPEs (6 μWm^{-3} on average), in agreement with the low average velocity of the upper crust (5.9–6.1 km/s).

Eastern Australia comprises the youngest portion of the Australian crust, which has been subjected to tectonic activity and thus to significant changes in the thermal state, since the Meso-Cenozoic. Most of the tectonic provinces composing these areas, such as the Delamerian and Lachlan orogens, exhibit elevated surface *HF* values (> 80 mW m^{-2}), which extend southward to most part of Tasmania. The southeastern margin of Australia, characterized by *HF* values between 55 and 89 mWm^{-2}, composes the Newer Volcanics Province (NVP), which takes this name from a chain of Cenozoic volcanoes located there. The significant *HF* variability was associated with recent intraplate volcanism (Mather et al., 2018). The Cenozoic volcanism can be related to edge-driven convection, triggered by the rapid lateral change of the lithospheric thickness (Fishwick and Rawlinson, 2012) or induced by mantle plumes (e.g., Hasterock and Gard, 2016). We can observe an eastwards sharp transition to intermediate surface *HF* values (50–60 mWm^{-2}), which characterize the New England Orogen, a tectonic feature of Phanerozoic age that does not show signs of crustal thermal perturbations.

2.3. Temperature variations in the crust and upper mantle

The obtained thermal model shows that the distribution of the temperature anomalies in the crust and upper mantle are quite different (Fig. 5a-b). Temperatures in the crust at a depth of 20 km range between about 200 °C and 700 °C and their patterns are correlated with those of the surface *HF* values. The variation of the heat generation with depth depending, in turn, on the seismic velocities (section 2.1, eq. 3), is the major factor responsible for the vertical gradient of the temperature within the crust. We observe that the western part of Australia, characterized by average temperatures of 200–250 °C, is divided from the central part of the continent, where the temperature sharply increases of 150 °C, by a zone few tens of kilometres wide (Fig. 5a). The broad zone of low temperatures includes the WAC and the surrounding provinces in the north and east, such as the Canning basin, Officer basin and the western part of the Eucla basin. Within this area, the higher temperatures (300–350 °C) are observed along the northwestern margin of the continent and in the western part of the Yilgarn craton, due to a more sialic crust, as suggested by the average crustal velocities (Fig. 3b-c, Section 2.2).

In the Proterozoic regions located east to the thermal boundary, we observe a large thermal anomaly (500–700 °C) in the northern part of the NAC, centered around Tennant Creek, which includes the Georgina basin and Mount Isa Inlier and elongates eastward up to the northeastern margin (Fig. 5a). This anomaly is the product of the high surface *HF* (Fig. 4) and high average velocity both in the upper and lower crust (> 6.3 km/s and > 7.0 km/s, respectively), which indicate that the heat generation is uniformly distributed within the crust. If the crust is more sialic in the first kilometres, where the velocity variations are not provided by the AuSREM model, the temperatures would be higher in the uppermost layer of the crust and less below. In the south, we observe several thermal anomalies (500–700 °C), corresponding to the eastern part of the SAC (eastern part of the Gawler craton and Curmarona province) and the Lachlan Orogen. These anomalies are divided

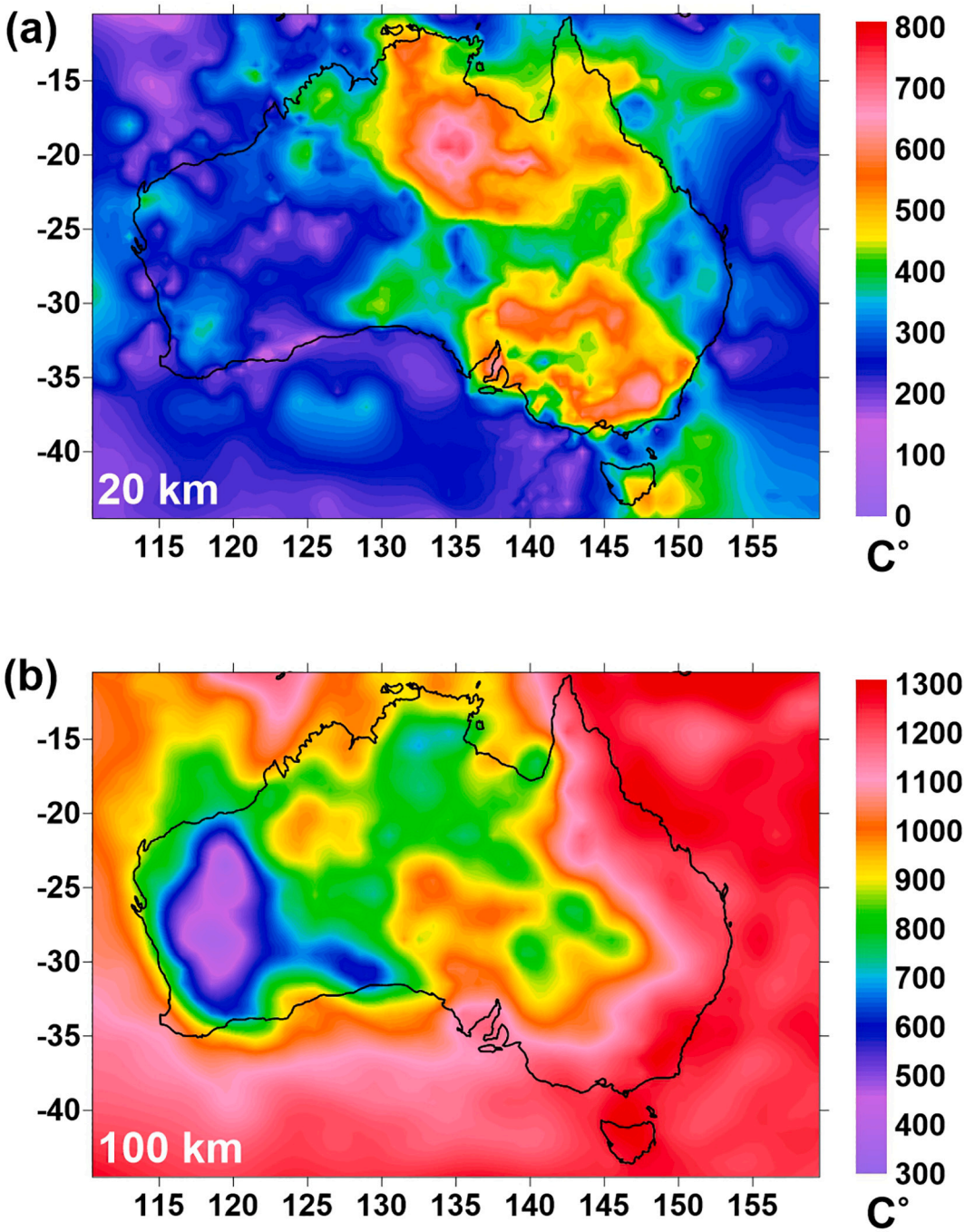

Fig. 5. (a-b) Temperature variations in the Australian plate, **(a)** in the crust at a depth of 20 km; **(b)** in the upper mantle at a depth of 100 km.

from those in the north by a zone crossing the central part of the continent, characterized by temperatures of 300–400 °C. These areas, corresponding to the Amadeus basin and the central part of the Eromanga basin, are less constrained by the surface *HF* data, which have values between 60 and 75 mWm^{-2} (Fig. 4). Furthermore, the upper crust is characterized on average by lower velocities than the surrounding regions (around 6.0 km/s, Fig. 3b, Section 2.2) around 6.0 km/s Fig. 3b, Section 3.2) and thus more heat generation confined in the uppermost layer of the crust. This has the effect to decrease the temperatures in the crustal levels below. On the other hand, in the NVP the temperatures vary quite heterogeneously between 400 °C and 600 °C, likely in relation to the volcanos' location (Fig. 5a). As in the surface *HF* map, we can also observe the sharp decrease in temperatures (250–400 °C) in the New England Orogen (Figs. 4 and 5a).

The temperatures variations in the upper mantle at a depth of 100 km span between about 400 °C and 1300 °C and are more correlated with the age of the lithosphere than with the surface *HF*. This result is not surprising, since the surface *HF* values more depend on shallow sources, such as those due to the presence of HPEs in the upper crust, as tectonic activity progressively redistributes elements at shallower depths. We can observe that the coldest regions are represented by the WAC, with the minimum located around the Yilgarn and Pilbara cratons (Fig. 5b). In this cool areas, the lithosphere thickens at least up to 250 km (Tesauro et al., 2020). The Proterozoic lithosphere is characterized by the temperatures between 700 °C and 900 °C, with the largest thermal anomalies (1000–1100 °C) located in the Canning and Amadeus basin. We can notice that the thermal crustal anomaly surrounding Tennant Creek, is not observed at the mantle depths,

indicating that its origin is in the crust.

In contrast, most of the SAC and East Australia, including the New England Orogen and Lachlan Orogen, show elevated temperatures (Fig. 5b) and in general a thinner and warmer lithosphere (Tesauro et al., 2020). This zone extends further to the East along the continental margin and southward beneath the Bass Strait and Tasmania. These thermal anomalies are associated with the Mesozoic rifting of the Tasman Sea and Southern Ocean, and also with the Cenozoic volcanoes. We can further notice that the high temperatures of the upper mantle of the Gawler craton are related to the intense reworking and refertilization occurred during the plate reorganization in the Mesoproterozoic (e.g., Aitken et al., 2016; Betts et al., 2016) and the Neoproterozoic orogenic events, which lead to the formation of the contiguous Delamerian Orogen (e.g., Williams and Betts, 2009). However, the sharp boundary observed in the surface heat flow map and crustal temperatures, which divides the Gawler craton into two parts (Figs. 4 and 5a), is not visible at the mantle depths. In general, the poor correlation between this uniform broad zone of mantle elevated temperatures with the heterogeneous crustal temperatures can be partly ascribed to the different resolution of these data sets. In the areas with high density of surface *HF* data, the *HF* map can resolve the thermal structures in more details than the seismic tomography. However, we should also consider that the thermal anomalies might be of different origin depending on their depths. In the crust, high temperatures are often related to high concentration of HPEs or partial melting, while in the mantle this can be the effect of passive or active asthenosphere uprising. Therefore, depending on the amplitude of the thermal anomaly, their genesis, and diffusion time, the temperatures can show different patterns at the crustal and upper mantle depths.

3. Strength model of the Australian plate

3.1. Method

The integrated lithospheric strength (σ_L) is estimated by vertical integration of the yield strength envelope (YSE). YSE predicts the maximum differential stress, which the rocks require before failure (Goetze and Evans, 1979):

$$\sigma_L = \int_0^h (\sigma_1 - \sigma_3) dz \tag{5}$$

where h is the lithospheric thickness and σ_1 and σ_3 are the maximum and minimum principal stresses, respectively. The crustal rocks can deform in the brittle or ductile conditions and the YSE provides the maximum rock strength given by the minimum of the two mechanisms of deformation. Therefore, the transition from the brittle to ductile conditions occurs at specific depths depending on temperature, strain rate, and rheology, as well as on the stress condition assumed (compression or extension). The brittle condition may be approximated by the Byerlee's law (Byerlee, 1978):

$$\sigma_b = f\rho g z(1 - \lambda) \tag{6}$$

where $\sigma_b = \sigma_1 - \sigma_3$ is the friction-related differential stress, f is a dimensionless parameter depending on the frictional coefficient and deformational regime (compression and extension condition), ρ is the density, g is the gravity acceleration, z is the thickness of each lithospheric layer, and λ is the pore fluid factor (Table 1). The average density has been obtained from a conversion of the seismic velocity of the AuSREM model, using the empirical relationship provided by Christensen and Mooney (1995) for the upper and lower crust, and the mineral physics approach of Stixrude (2005) for the upper mantle. The power-law dislocation creep, describing the ductile deformation (σ_d), is estimated according to Goetze and Evans (1979):

$$\sigma_d = \left[\frac{\dot{\varepsilon}}{A_P}\right]^{\frac{1}{n}} . \, exp\left[\frac{E_P}{nRT}\right] \tag{7}$$

where $(\sigma_d) = \sigma_1 - \sigma_3$ is the ductile-related differential stress, $\dot{\varepsilon}$ is the strain rate, A_P is the power strain rate, n is the power law exponent, E_P is the power law activation energy, R is the gas constant, and T is the temperature (Table 1). At high stress and relatively low temperatures conditions (< 1000 °C), which are usually present in the uppermost mantle, rocks deform in ductile conditions, following the Dorn law. We used the results of Demouchy et al. (2013) that have derived the exponential flow law for a "dry olivine" from laboratory experiments (Eq. (4)), which are applicable to the uppermost mantle.

$$\sigma_d = \sigma_D\left(1 - \left[-\frac{RT}{E_D} . \, ln\left(\frac{\dot{\varepsilon}}{A_D}\right)\right]^{1/2}\right)^2 \tag{8}$$

where σ_D is the Dorn law stress, E_D is the Dorn law activation energy, and A_D is the Dorn law strain rates (Table 1). The rheological parameters of the crust have been defined according to the rheological model described in section 3.2. Other input parameters used for the ductile strength calculations are the thermal model of the crust and upper mantle (section 2.3) and the strain rate model (section 3.3).

3.2. Rheological model of the crust

As was demonstrated in the previous section, the strength depends on the ductile deformation of the rocks, which is described by the values of the creep parameters that have been obtained from laboratory experiments conducted on natural samples (e.g., Goetze and Evans, 1979; Carter and Tsenn, 1987; Wilks and Carter, 1990). More recently, other laboratory experiments have been carried out on simple monophase synthetic minerals having a homogeneous grain size (Bürgmann and Dresen, 2008). However, the extension of the results of these experiments to real rocks has not yet been demonstrated, especially considering impurity usually present in the natural aggregates and absent in the synthetic materials. This might be one of the main sources of the dislocations exploited by dislocation creep. For this reason, we prefer to use the results of the laboratory experiments conducted on natural rocks than on synthetic material. Unfortunately, these results refer to a limited amount of rocks' types, having sialic (e.g., quartzitic, dioritic, and granitoid rocks) or mafic composition (e.g., diabasic and granulitic rocks). Therefore, we chose the rheology of the upper and lower crustal layer, considering that the above mentioned rocks are characterized by different seismic velocities, in particular, sialic rocks have lower seismic velocities and weaker rheology than those having a mafic composition (e.g., Christensen and Mooney, 1995). Considering the velocity ranges in the upper and lower crust (Fig. 3b-c), we assigned the rheology of 'dry quartzite' and 'dry granite' (Carter and Tsenn, 1987) to the rocks of the upper crust, having the average *Vp* lower and higher than 6.0 km/s, respectively (Fig. 6a, Table 1 and Table 2). In contrast, we associated the rheology of 'wet diorite', 'dry diabase', and 'mafic granulite' (Carter and Tsenn, 1987; Wilks and Carter, 1990) to the rocks of the lower crust with the average *Vp* lower than 6.6 km/s, between 6.6 km/s and 7.0 km/s, and higher than 7.0 km/s, respectively (Fig. 6b, Table 1 and Table 2). We do not assign any rheology to the sediments, because they usually are affected by only brittle deformation, due to their low depths of deposition. Based on these conditions, we obtained six combinations of the crustal rheology (Fig. 6c, Table 2). The first two combinations represent the crust having low seismic velocities and thus weak rheology, which is mainly present in the offshore areas. The third and fourth combination corresponds to the weak and stiff rheology of the upper and lower crust (or viceversa stiff and weak rheology), respectively, which mostly characterize the continental margins or very small parts of the continental areas (e.g., the southeastern part of the Eucla basin). The fifth and sixth combinations,

Table 1
Rheological model parameters.

Parameter	Symbol	Units	Sediments	Upper crust	Lower crust	Upper mantle
Composition	–	–	–	Quartzite (dry)[1]/ Granite(dry)[1]	Mafic-Ganulite[2]/ Diorite (wet) [1]/ Diabase (dry)[1]	Olivine PL(dry) [3] Olivine DL(dry) [4]
Density min-max/mean	ρ	km/m^3	1900–2700/ 2247	2517–3160/ 2697	2515–3232/ 2918	3421–3474/3446
Layer Thickness min-max/mean	z	km	0–11/1.0	1.5–31.5/14.1	1.0–21.5/10.0	7.5–281/151
Friction Coefficient ext/com conditions	f	–	0.75/3	0.75/3	0.75/3	0.75/3
Pore fluid factor	λ	–	0.36	0.36	0.36	0.36
Power law exponent	n	–	–	2.72/3.3	4.2/2.4/3.05	3
Power law activation energy	Ep	KJ mol^{-1}	–	134/186	445/212/276	510
Power law strain-rate	A_p	Pa^{-n}s^{-1}	–	6.03×10^{-24}/ 3.16×10^{-26}	8.83×10^{22}/1.26×10^{-16} /6.31×10^{-20}	1.2589×10^{-12}
Dorn law activation energy	E_D	KJ mol^{-1}	–	–	–	320
Dorn law strain-rate	A_D	s^{-1}	–	–	–	1.4×10^{-19}
Dorn law stress	σ_D	Pa	–	–	–	5.9×10^{9}

distinguished by the rheology of the lower crust, mostly correspond to the continental areas generally characterized by the high velocity and stiff rheology.

We can observe that there are regions of low *HF* and crustal temperatures, such as the eastern part of the WAC and the Officer basin, which are characterized by high velocity and thus stiff rheology (sixth combination), due to the mafic composition of the crust. At the same time, in the western part of the WAC the lateral increase of the crustal temperature is accompanied by the decrease of seismic velocity and correspondingly by a weaker rheology (fifth combination).

On the other hand, there exist tectonic provinces, such as the NAC and the New England Orogen, in which the correlation between the lateral variations of the crustal rheology and temperature is not significant. In particular, we can observe that in the Tennant Creek and Arunta Block the rheology is very stiff (sixth combination, Table 2, Fig. 6c), on account of the mantle underplating, which produced a thick mafic lower crust (e.g., Clitheroe et al., 2000). However, this area is also characterized by high values of *HF* and elevated crustal temperature (Fig. 4 and 5a). If the HPEs are prevalently concentrated in the uppermost part of the crust, making it more differentiated than what we assumed using the empirical equation of Chapman (1986), the temperature in the lower crust would be overestimated. On the other hand, Hasterock and Webb (2017) noticed that the higher median heat production in Proterozoic Australia is in the same seismic range as in North America. Therefore, they suggested that the heat production is due to crustal enrichment that likely extends vertically throughout the crust (and possibly the entire lithosphere). This hypothesis can explain the elevated temperature, without ruling out the possibility of a mafic lower crust.

3.3. Strain rate model

As discussed in section 3.1, the ductile deformation, controlled by dislocation creep and low-temperature plasticity, strongly depends on strain rates. Estimates of lateral and vertical variations of this parameter are crucial for a robust calculation of the YSEs. Since the plate tectonics is driven by many forces including large-scale mantle flows, only a global mantle convection model can provide these estimates. The model has to include rigid plates, weak plate boundaries, realistic densities, and a viscosity distribution for the whole mantle. To verify the dynamic model, we used the plate velocity model NRR-MORVEL56 (Argus et al., 2011) that provides homogeneous coverage for the whole area. To calculate present-day mantle flow velocities, we solve the Navier-Stokes equation together with the Poisson equation satisfying the momentum and mass conservation conditions. The numerical code ProSpher is employed to estimate mantle flow velocities (Petrunin et al., 2013; Kaban et al., 2014). The ProSpher code combines the advantages of both spectral-based and FD/FE methods, providing a way to account for strong lateral viscosity variations (up to 5 orders of magnitude laterally), self-gravitation and compressibility. The full method and setup are described in detail in Petrunin et al. (2013) and Kaban et al. (2014).

The strain rate variations at the depths 100 km and 200 km span in a range between 10^{-16} and 10^{-14} s^{-1} (Fig. 7a-b). At a depth of 100 km, the strain rate values show in general a progressive increase from west to east, which expresses a decrease of rigidity and corresponds to the age decrease of the tectonic features. At a depth of 200 km, there exists a sharper division between the more rigid cratonic regions, showing the strain rate values lower than 10^{-15}, which reflect their long-term stability, and the more deformable Phanerozoic features with the strain rates from 10^{-15} to 10^{-14}. The largest values of the strain rates are localized along the continental eastern margin, corresponding to the youngest provinces tectonically active since the Mesozoic (Fig. 7b).

3.4. Strength variations in the Australian lithosphere

The integrated strength of the lithosphere, crust and upper mantle parts of it, together with the percentage of the crustal strength are displayed in Fig. 8(a-d). Furthermore, we calculated the strength variations along three cross-sections (Fig. 8e). All the parameters are calculated for both deformational regimes (Table 1), but we display and discuss only the results for the compressional stress condition. We display over the map of the integrated crustal strength (Fig. 8b) 1136 intraplate seismic events taken from the USGS seismic catalog (https://earthquake.usgs.gov/earthquakes/search/). The earthquakes occurred from 1990 to present-day having the moment magnitudes (Mw) > 2.5. The distribution of the integrated lithospheric strength is mainly influenced by the lateral variations of temperatures, in particular the sharp transition between the strong (integrated strength > 10^{13} Pa m) and less rigid areas (integrated strength < 10^{13} Pa m) (Fig. 8a-c). The strain rate variations (Fig. 7a-b), with respect to the average value of 10^{-15} s^{-1}, used in previous studies (e.g., Tesauro et al., 2015), decrease the strength in the cratonic areas and increase it in the eastern continental margin. Therefore, the strain rate variations should partly compensate the effect of temperatures. However, they span in a small range (10^{-16}-10^{-15} s^{-1}) and do not significantly influence the strength values.

Very high values of the integrated lithospheric strength (> 5 10^{13} Pa m) are observed in several tectonic provinces of Precambrian age, located in the western part of the Australian plate, such as the northern and eastern part of the Yilgarn craton, the eastern part of the Capricorn Orogen, the Pilbara craton, the Albany–Fraser Province, the western part of the Officer and Eucla basin, and the southern part of the Canning basin, with the maximum values located in the Yilgarn craton

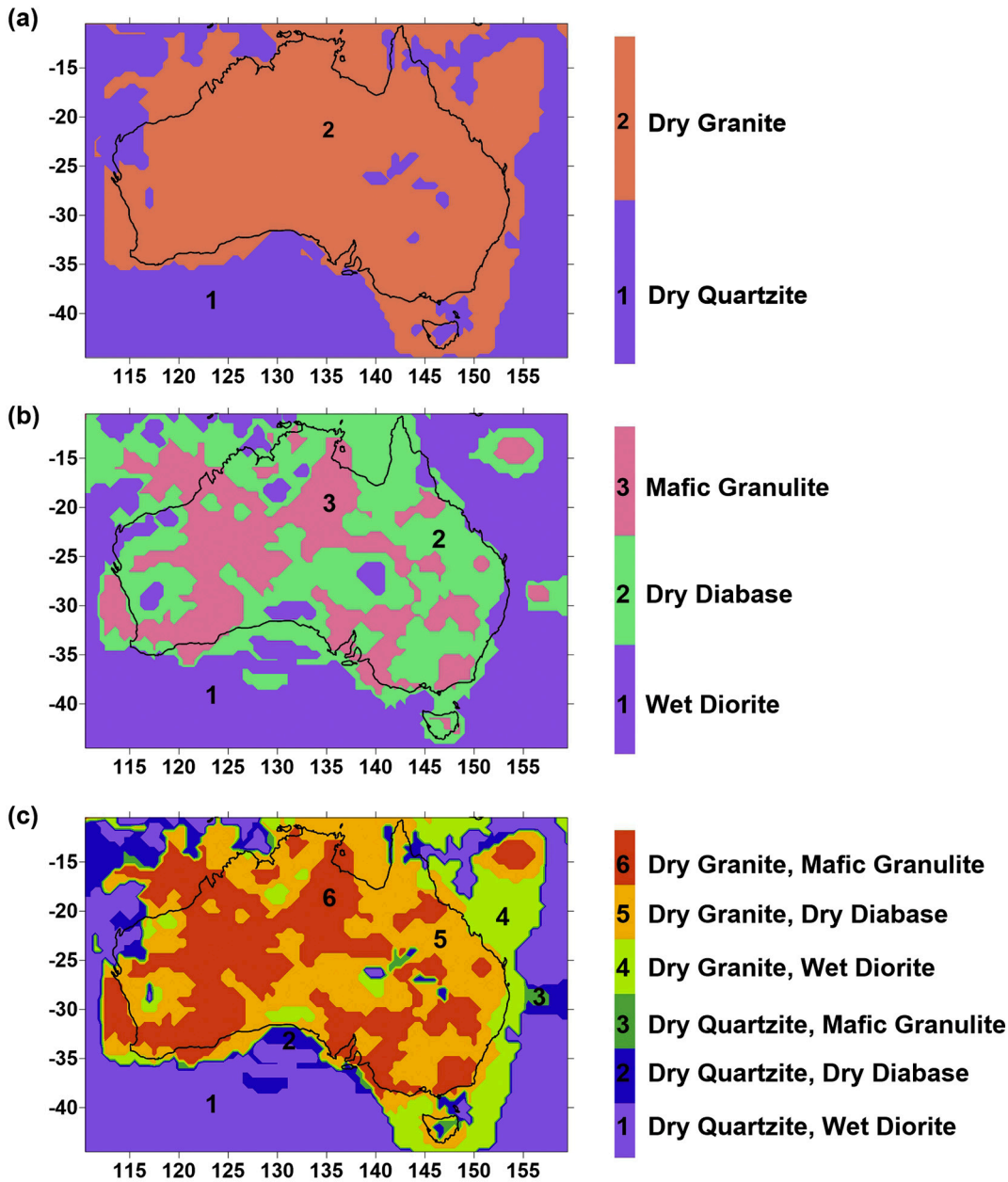

Fig. 6. (a-c) Rheological types, assigned on the basis of the crustal seismic velocity variations estimated by AuSREM model, for **(a)** upper crust; **(b)** lower crust; **(c)** crust derived by the combination of the rheological types of the upper and lower layer. Black numbers indicate the rheological types associated to the seismic velocity ranges displayed in Table 2.

and Capricorn Orogen. The integrated lithospheric strength remains high also in the surrounding regions ($> 10^{13}$ Pa m). In these areas, the strength partition between the crust and mantle lithosphere is quite heterogeneous (Fig. 8d). Both cratons composing the WAC retain less than 30% of the strength in the crust, while in the surrounding regions the percentage of the crustal strength sharply increases to 50% or even 80% in the Officer basin. These results indicate that most of the WAC is characterized by a strong mantle lithosphere, with maximum values located in the central region of the Yilgarn craton (Fig. 8c) At the same time, its crust, retaining high strength (10^13 Pa m, Fig. 8b), is less cold and strong than in the surrounding areas (Fig. 8b). The largest values of the crustal strength (5 × 10^13 Pa m, Fig. 8b) are found in the Officer basin, Musgrave Province, and in the southern part of the Canning basin, reflecting low temperatures and high rigidity of the crust. We can also observe that the intraplate earthquakes in the western part of Australia do not show a strong correlation with the edges of the cratons, as observed in previous studies for the Siberian, North America, and Congo craton (Craig et al., 2011; Mazzotti, 2007; Sloan et al., 2011). However, many seismic events occur in the areas characterized by a weak crust, such as the southwestern part of the Yilgarn craton, while some others are located along the transition zones between the weak and strong crust, as those at the margins of the Officer basin and Musgrave Province. The high concentration of seismicity in the zones of sharp lateral variations in the crustal strength has been noted already for other continental plates, e.g. in North America (Mooney et al., 2012; Tesauro et al., 2015).

Eastward, there is a sharp boundary between the areas having high ($> 10^{13}$ Pa m) and low values ($< 10^{13}$ Pa m) of the lithospheric strength, which crosses the central part of Australia. This boundary divides the NAC characterized by a weak lithosphere, from the stronger Ngalia and Amadeus basin and Musgrave province in the south. In the NAC the weakest area corresponds to Tennant Creek, characterized by

Table 2
Rheological code and Young's Modulus (*E*) assigned to the Upper (UC) and Lower Crust (LC), according to the corresponding velocity range taken from AuSREM model. The rheological types from 1 to 6 are assigned, considering a crustal division into two layers. Creep parameters of the rheology assigned are displayed in Table 1.

Code	Velocity (km/s) UC	Velocity (km/s) LC	Rheology/E (GPa) UC	Rheology/E (GPa) LC
1	5.50–6.0	< 6.60	Dry Quartzite/93	Wet Diorite/99
2	5.50–6.0	6.60–7.0	Dry Quartzite/93	Dry Diabase/106
3	5.50–6.0	> 7.0	Dry Quartzite/93	Mafic Granulite/110
4	> 6.0	< 6.60	Dry Granite/88	Wet Diorite/99
5	> 6.0	6.60–7.0	Dry Granite/88	Dry Diabase/106
6	> 6.0	> 7.0	Dry Granite/88	Mafic Granulite/110

high *HF* and temperatures (Figs. 4 and 5a-b). Its crust, although characterized by the stiffest rheology (sixth combination, Fig. 6c), is sufficiently hot to decrease the crustal strength to less than 10^{13} Pa m (Fig. 8b). Southward, the strength boundary passes along the eastern border of the Amadeus basin, Musgrave province, and Officer basin, and crosses the SAC, dividing the Gawler craton into two parts. The eastern part of the Gawler craton is weaker, likely because its lithosphere has been affected by extension and thinning caused by the upwelling of a mantle plume during the Neoproterozoic (Zhao et al., 1994). This main division is also visible in the integrated crustal strength (Fig. 8b), while for the mantle lithosphere, it is shifted westward and the weak zone comprises the entire SAC. Such a difference between the crust and mantle lithospheric strength is mainly due to their different thermal conditions since the crust is characaterized by intermediate temperatures (Fig. 5a) and the shallow upper mantle is anomalously hot (Tesauro et al., 2020). We can further observe that in most of the NAC and SAC the crust retains more than 80% of strength, despite its weakness. These results indicate that the upper mantle is

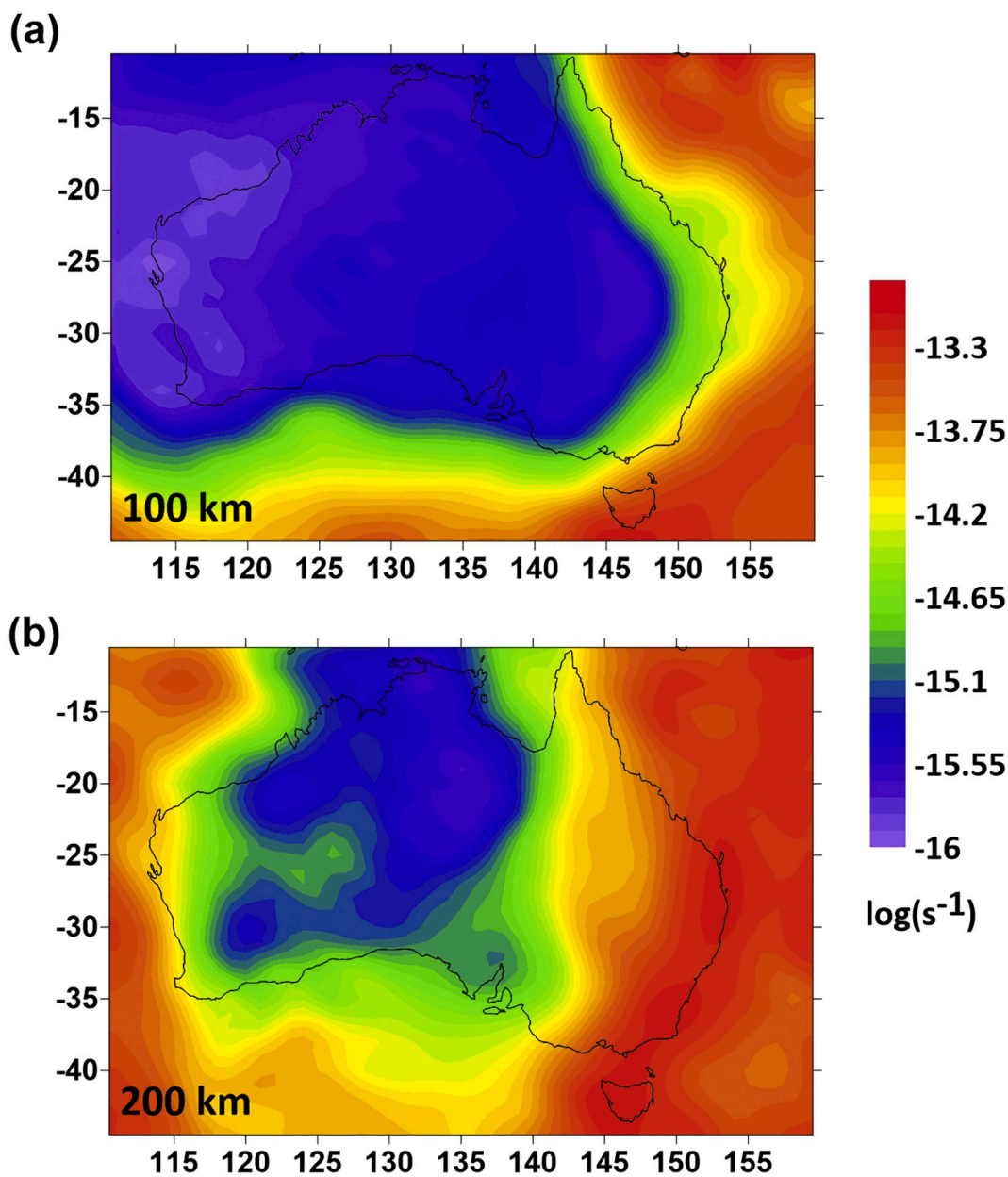

Fig. 7. (a-b) Variations of the second invariant of the strain rate tensor (s^{-1}) at a depth of **(a)** 100 km and **(b)** 200 km.

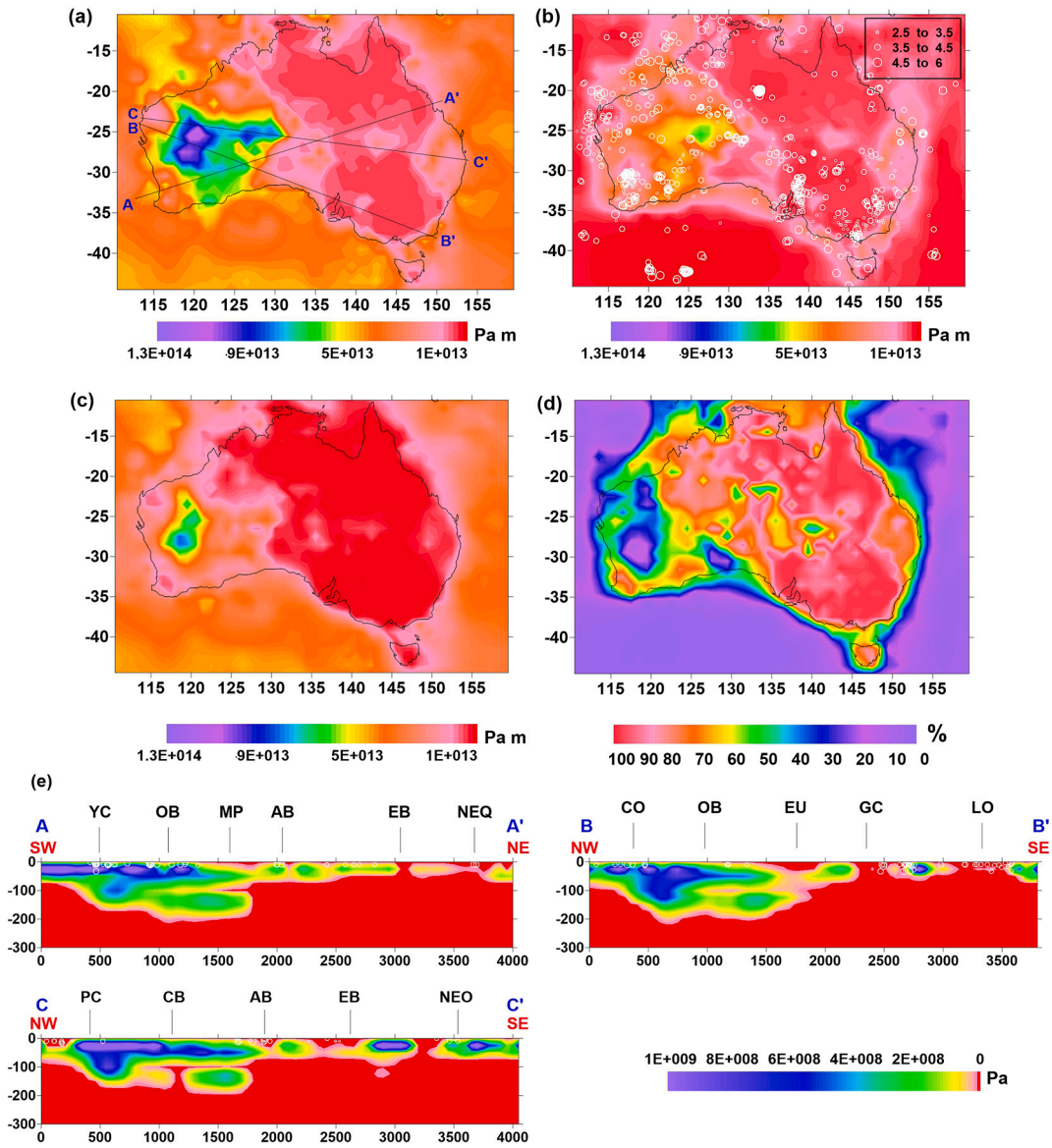

Fig. 8. (a-e) Integrated strength (Pa m) and strength (Pa) variations along three cross-sections. Horizontal and vertical axes of the cross-sections display the distance and depth (both in km), respectively. **(a)** Integrated strength of the lithosphere. The three black lines show the location of the cross-sections; **(b)** Integrated strength of the crust. White circles show the earthquakes location, occurred from 1990 to present-day, with moment magnitudes (Mw) > 2.5, taken from the USGS seismic catalog (https://earthquake.usgs.gov/earthquakes/search/); **(c)** Integrated strength of the mantle lithosphere; **(d)** Percentage of crustal strength; **(e)** Strength variations along three cross-sections (A-A′, B-B′, and C-C′, respectively).

very weak and that the strength is distributed according to a crème brûlée model (strong crust underlain by a weak mantle, Jackson, 2002), which implies that the region is unstable on a long-time scale (François et al., 2013).

Lateral strength distribution along three cross-sections (Fig. 8e) shows the presence of a rigid lithosphere, extending up to a depth of 150–200 km in the WAC and surrounding basins. Westward, this layer is reduced to about 70 km along the continental margins, and eastward along the western boundary of the NAC and SAC. Therefore, there is no strict relationship between the strength distribution and age of the tectonic provinces, indicating that the originally strong Proterozoic mantle lithosphere of the NAC and SAC has been replaced or refertilized (Tesauro et al., 2020).

The tectonic provinces of Phanerozoic age, located east to the NAC and SAC, are generally characterized by low total integrated strength, which is mainly (> 80%) concentrated in the crust (Fig. 8d). This area includes the Delamerian and Lachlan orogen in the south, close to the Gawler Craton, and the regions affected by recent volcanism (NVP), characterized by a hot lithosphere. In the north, the central part of the Eromanga basin retains more strength in the crust, on account of its lower temperature (Figs. 5a, 8b and d, cross-section C-C′) and causes a partial division between the weak zones located north and south of it.

We can clearly distinguish the New England Orogen from the other Phanerozoic provinces, which is characterized by a higher amount of strength mainly in the crust (about 10^{13} Pa m), due to its lower temperatures with respect the surrounding tectonic provinces (Figs. 5a, 8a-b, and e, cross-section C-C′). We can further observe that although most of the Australian plate east to the main strength boundary is weak, the distribution of the earthquakes is uneven, having a high concentration in the southern part of the Curnamona Province, coinciding with the NVP, a strongly active tectonic region. On the other hand, most of the NAC is almost aseismic. The absence of seismicity might be an indication of the tectonic stability of the area, as well as due to the presence of a very weak crust that prevents earthquakes nucleation.

4. Effective elastic thickness (*Te*) model

4.1. Method

The effective elastic thickness (*Te*) is the geometric measure of the flexural rigidity of the lithosphere, which describes the resistance to bending under vertical loads. It is primarily related to the combined effects of rheological and thermal heterogeneity of the lithosphere and reflects the integrated effect of all competent layers that are involved in the support of a load, including the weak ones (e.g., Burov and Diament, 1995).

In the continental areas, *Te* spans in a large range from 5 to over 100 km, depending on the strength and coupling-decoupling conditions of the lithospheric layers. We estimated the *Te* as a function of the thickness of the mechanically strong layers (Δh_i), which is defined as the vertical distance between its top and bottom, for the coupling conditions:

$$T_e^{(n)} = \left(\sum_{i=1}^{n} \Delta h_i\right) \tag{9}$$

or between its top and the depth at which the yield stress computed decreases below a threshold of 10 MPa (e.g., Ranalli, 1994), in case of decoupling conditions:

$$T_e^{(n)} = \left(\sum_{i=1}^{n} \Delta h_i{}^3\right)^{1/3} \tag{10}$$

Decoupling conditions occur when weak ductile zones in the crust or between the crust and mantle do not allow horizontal stresses to be transferred between the lithospheric layers (Fig. A1). As a result, there exist several 'elastic' cores inside the bending plate. In such a multilayer plate, the stresses are reduced, for the same amount of flexure, compared to a single plate. Consequently, *Te*, which reflects the combined strength of all brittle, elastic, and ductile layers, is also reduced (Eq. (10)), compared to a mono-layer plate with coupling lithospheric layers (Eq. (9)).

In the calculation, we took into account variations of the Young's Modulus (*E*) with depth (Tesauro et al., 2012) not considered by Burov and Diament (1995), using different *E* values for each crustal rheology and a constant value of 180 GPa for the upper mantle (Appendix A1), as displayed in Table 2. However, since the value of the mantle *E* is almost doubled compared to previous models (70–100 GPa), the *Te* values are also greater than those calculated by Burov and Diament (1995). Therefore, when we discuss the results (section 4.3), we assume that the areas characterized by high rigidity should have $Te > 100$ km, due to the presence of a thick strong upper mantle layer.

4.2. Coupling-decoupling conditions

The vertical strength distribution defines three main conditions (Fig. 9a): (1) all the lithospheric layers are coupled (fully coupling conditions); (2) all the lithospheric layers decoupled (fully decoupling conditions); (3) the crustal layers are coupled and the crust is decoupled from the upper mantle (partial decoupling conditions). We can observe that most of the WAC and surrounding Proterozoic provinces (e.g., the Canning basin and western part of the Officer basin), as well as most of the New England Orogen in the eastern part of the continent, are characterized by fully coupling conditions. The transitions between the areas showing fully coupling conditions from those characterized by partial or fully decoupling conditions correspond to the boundaries dividing the areas having high and low integrated lithospheric strength (Figs. 9a and 8a). The fully coupling conditions in the western part of the Australian plate are determined by a combination of the relatively low temperature in the shallow lithosphere and strong crustal rheology. We can notice that in this case, the crustal thickness (Fig. 3a) does not influence strongly the coupling/decoupling conditions like the other parameters. Indeed, there is a little part of the Yilgarn craton, in which the crust is decoupled from the upper mantle, although its thickness is less than 35 km, while the fully coupled conditions are present also in the areas, where the Moho depth is over 45 km (e.g., in the Musgrave province). In contrast, in the New England Orogen fully coupling conditions are present, although the lower crust has weaker rheology and higher temperature. These conditions are determined by the crust, which is thin enough (less than 40 km, Fig. 3a) to prevent its decoupling from the upper mantle due to the high temperatures. The partial and fully decoupling conditions presented in other parts of the Australian plate are mainly due to the high crustal temperatures and only slightly correlated with the rheology and crustal thickness variations (Figs. 5a, 3a, and 6a-c). The Eromanga basin is mainly characterized by partial decoupling conditions or fully coupling conditions and divide two large areas of fully decoupling conditions. The first one in the north corresponds to the NAC, mostly surrounded by areas having partial decoupling conditions, while the other in the south, including Curnamona Province and Lachlan Orogen, is connected to an area of partial decoupling conditions, mainly corresponding to the Eucla basin. On the other hand, in the Gawler craton, the transition from fully coupling to fully decoupling conditions occurs in its central part.

4.3. Effective elastic thickness variations

The values of *Te* are more uniformly distributed than the integrated strength, due to their dependency on the coupling/decoupling conditions (Figs. 9a-b). The contribution given by the thickness of each mechanically strong layer of the crust (M_{uc}, M_{lc}) and upper mantle (M_{mantle}) are displayed in Figs. 10(a-c) The greatest values ($Te > 100$ km) are found in the WAC and extend eastward to most of the Officer and western part of the Eucla basins. They mostly correspond to the areas showing fully coupling conditions, characterized by a large thickness of the M_{mantle}.

High values (*Te* between 70 and 100 km) are found in the north, in the Canning basin, and in the western part of the Amadeus and Musgrave Province (Fig. 9b). Therefore, although these provinces retain more than 60% of the strength in the crust, their lithosphere is quite rigid. The sharp transition between the rigid western part and the less rigid central and eastern part of the Australian continent ($Te < 50$ km) corresponds to the boundary dividing the same areas having high and

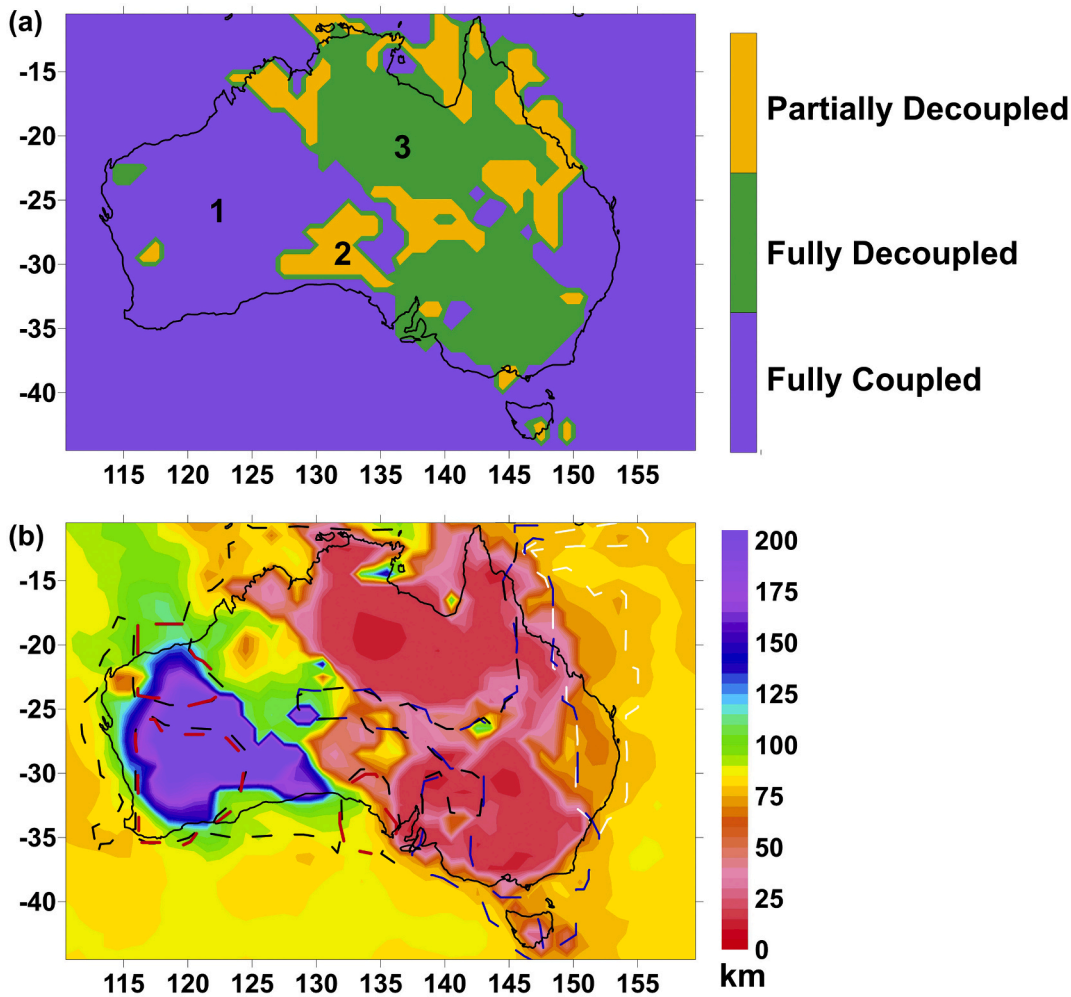

Fig. 9. a-b (a) Coupling/decoupling conditions. Black numbers stand as follows: **1**, All the lithospheric layers are coupled; **2**, all the lithospheric layers are decoupled; **3**, Upper and lower crustal layers are coupled and lower crust is decoupled from the upper mantle; **(b)** Effective elastic thickness (km), *Te*. Colored dash lines define the regions with different age as follows: Archean (red), Proterozoic (black), Paleozoic (blue), Meso-Cenozoic (white).

low integrated mantle lithosphere (Fig. 8c). However, we can observe that also within the zones of low rigidity there are areas having very high (~100 km) or high (~70 km) *Te* values, such as the central part of the Eromanga basin and the New England Orogen, respectively. These results look quite different from those obtained in the previous study of Swain and Kirby (2006), in which *Te* is estimated using a wavelet coherence method. According to this study, the largest *Te* values (~100 km) form a sub-circular zone, which includes Central Australia and extends northwards over the continental shelf. However, it seems unlikely that the most rigid part of the plate corresponds to the area where the uppermost mantle is characterized by low seismic velocities related to a thermal anomaly or low-density mineral phase (Tesauro et al., 2020). Previosuly, Zuber (1989) derived the *Te* based on the coherence of the 2D Fourier transforms of the Bouguer gravity anomalies and topography. Their results show sharp variations of the *Te* values along the Tasman line, dividing Precambrian Western and Phanerozoic eastern Australia. They interpreted this transition as related to the time of the lithospheric stabilization. For the cratonic regions with the *Te* values between 90 and 130 km, it occurred in the Proterozoic and during the Paleozoic or later in the eastern terranes with the *Te* values between 15 and 75 km. However, these results suffer from the choice of the size of subregions, for which the *Te* is calculated. In particular, the large subregions might have variable rigidity, and thus the calculated *Te* values are only partly representative. Our results are instead weakly correlated with the age of the tectonic provinces (Fig. 9b). Although most of the maximal *Te* values are observed in the Archean cratons, as in Zuber (1989), their relation to the age of the crystalline crust (Mooney et al., 2012), show that the *Te* values span in a similar range with large standard deviation (Table 3). This means that each age group includes terranes of different rigidity, which reduces the correlation. This supports the hypothesis that parts of the lithosphere, composing the old terranes, have been heated/metasomatized and thus weakened after the Precambrian stabilization (Tesauro et al., 2020).

Looking at the thickness of the mechanically strong part of the lithospheric layers, we can notice that in many regions the *Te* values (Fig. 9b) are strongly correlated with those of the M_{mantle}, which spans

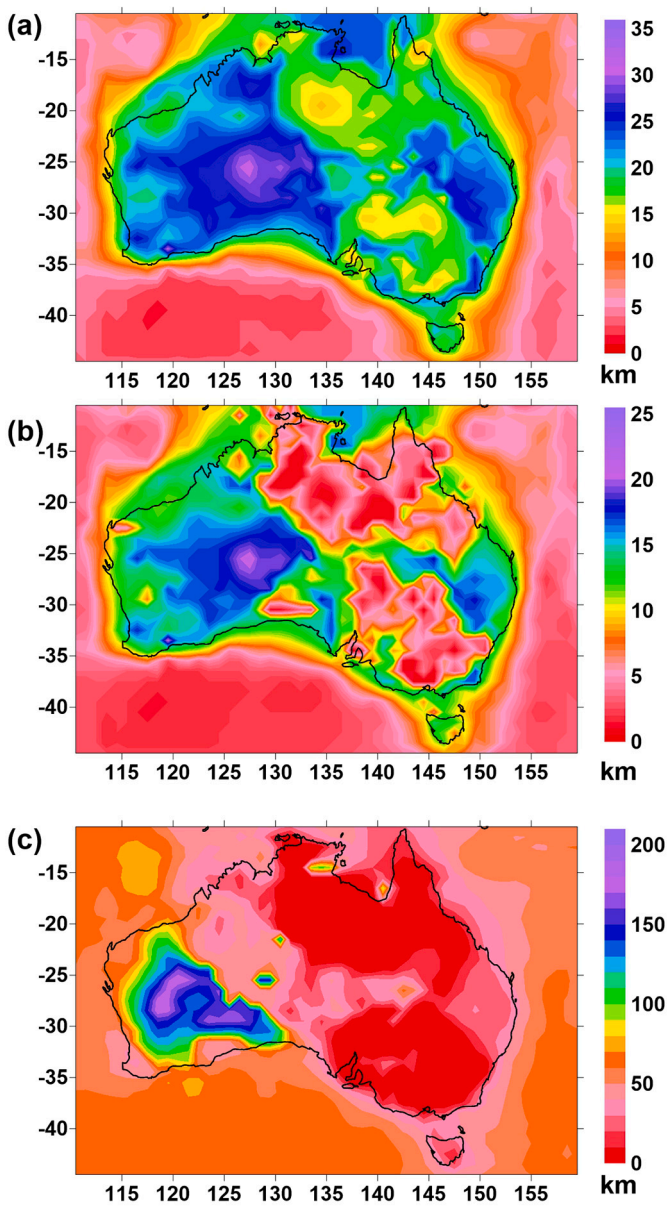

Fig. 10. (a-c) Thickness (km) of the **(a)** mechanically strong upper crust, M_{uc}; **(b)** mechanically strong lower crust, M_{lc}; **(c)** mechanically strong upper mantle, M_{mantle}.

Table 3
Range, mean, and standard deviations of the *Te* with respect to the age of the crystalline crust.

Age	Min (km)	Max (km)	Mean (km)	STD (km)
Archean	14	254	102	50
Proterozic	13	260	72	48
Paleozoic	14	239	87	36
Meso-Cenozoic	15	251	67	46

from more than 100 km to 0.5 km (Fig. 10c) and less with the integrated strength of the lithospheric mantle (Fig. 8c). This is because the high M_{mantle} /*Te* values are presented also in the eastern part of the Officer and Eucla basin, having the integrated strength of the lithospheric mantle less than 5×10^{13} Pa m (Fig. 8c). Indeed, the continuous and smooth increase of the temperature with depth in these regions results in an increase of the thickness of the M_{mantle}, but not of the strength, as occurs in the Yilgarn craton, characterized by a thick cold upper mantle layer (Tesauro et al., 2020), with a sharp temperature variation at its base.

The M_{mantle} is negligible (less than 1 km) in most of the SAC and Lachlan orogen, as well as in the central and eastern provinces of the NAC (e.g., Tennant Creek and Arunta Block). The M_{uc} and M_{lc} span in a smaller range in comparison with the M_{mantle} (15–31 km and 0.5–21 km, respectively), but both of them give a contribution to *Te* greater than 15 km in a half part of the continental plate (Fig. 10a-b). Their lateral variations are more influenced by temperature than by rheology variations (Figs. 5a and 6a-b), with the greatest values, centered over the Officer basin and Musgrave Province, the areas characterized by low *HF* and crustal temperatures (Figs. 4 and 5a).

Furthermore, in the Tenant Creek and Arunta Block and in the southern part of the Lachlan orogen, the M_{lc} shows negligible values (< 1 km), despite the stiff rheology assigned (sixth combination, Fig. 6c, Table 2). In contrast, the influence of the weak rheology associated with the lower crust is visible in the southern part of the Eucla basin (fourth combination, Fig. 6c, Table 2), where the values of the M_{lc} are lower than 1 km despite the moderate crustal temperatures (Fig. 5a). The significant reduction of the M_{lc} is responsible for decoupling of the crust from the upper mantle (Fig. 9) and a strong decrease of the *Te* (Fig. 9b). Therefore, these features are less tectonically stable and can experience lower crustal flow.

5. Influence of the input parameters on the strength and effective elastic thickness

To evaluate potential uncertainties of the results, we analyze three alternative strength and *Te* models (Figs. 11 and 12). In the first one, we assumed an average constant value of the strain rate equal to 10^{-15} s^{-1}, considering that it may vary from $\sim 10^{-13}$ s^{-1} (for the fast deforming areas) to 10^{-17} s^{-1} (for the cratonic stable areas). In the second and third models we employed uniformly weak (Type 1, Table 2) and stiff rheology (Type 6, Table 2), respectively, leaving all other parameters unchanged.

Since the variations of the strain rates values of the model displayed in section 3.3 at a depth of 100 km (Fig. 7a) relative to the uniform value (10^{-15} s^{-1}) are relatively small (up to one order of magnitude in the on-shore areas), the results of the first alternative model are very similar to those already discussed (Figs. 11a-d and 12a-b). In particular, the differences in the strength and *Te* between the cratonic and Phanerozoic areas become smaller when the strain rates are constant (Figs. 11a-d and 12b). We do not discuss the effect of the strain rates variability above 100 km depth, since the strength becomes negligible, due to the high temperatures.

In contrast, the assumption of uniform crustal rheology has a greater impact on the strength and *Te* (Figs. 11e-n and 12c-f). In the model with "stiff" crustal rheology, the small values of the integrated strength are limited to the hottest areas of northeastern and southeastern Australia, where the percentage of the crustal strength is close to 100% (Fig. 11h). The use of the "stiff" rheology produces the full coupling conditions in the areas characterized by the intermediate coupling conditions in the original model (Fig. 9a), with consequent increase of the *Te* (Fig. 12c-d). The use of the "weak" rheology produces a significant strength decrease in most parts of the continental area. The great values of the integrated strength are now limited to the Yilgarn craton, where the percentage of the crustal strength decreases to less than 10% in the

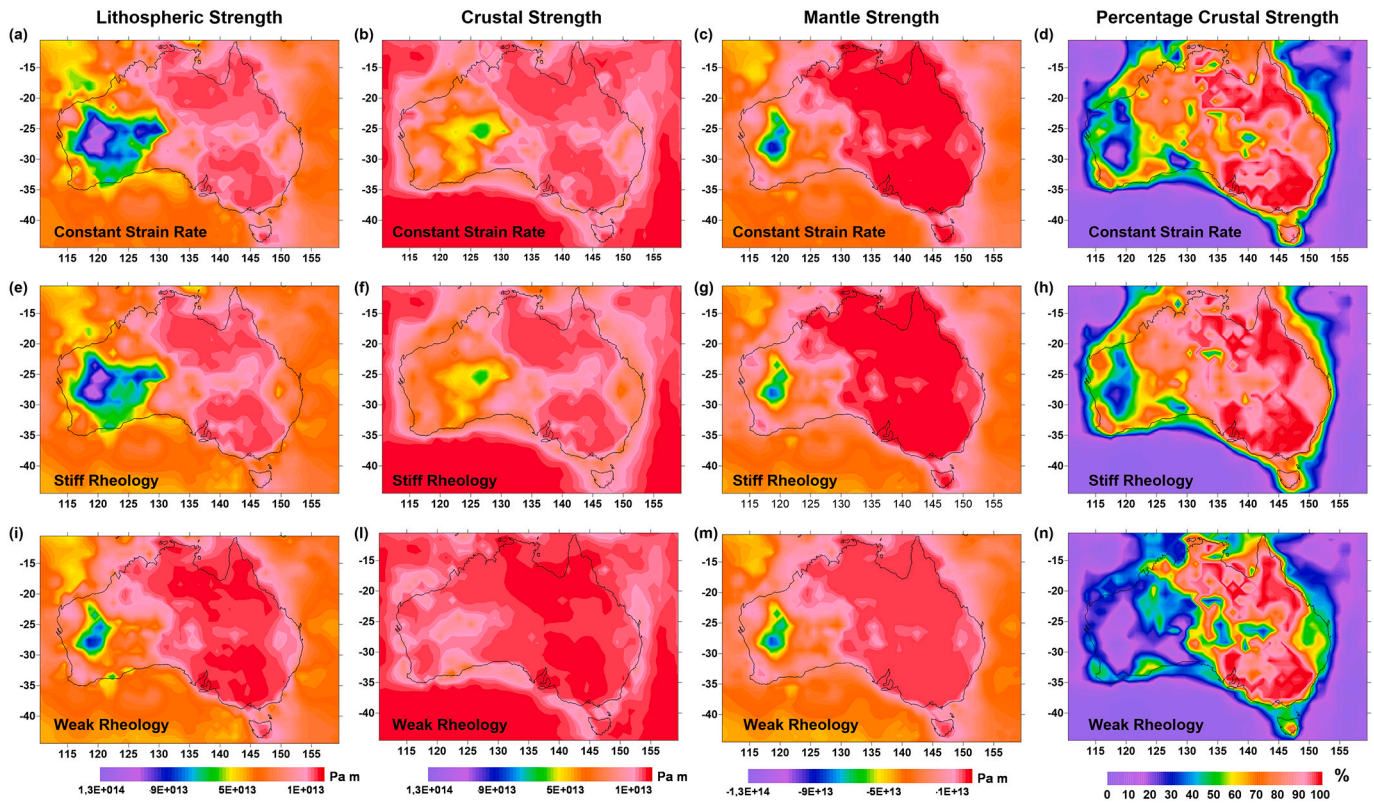

Fig. 11. Additional models of integrated strength for **(a-c)** the lithosphere, crust, mantle lithosphere, and **(d)** percentage of the crustal strength, using a fixed value of strain rates (10^{-15} s^{-1}); **(e-h)** as before for the stiff crustal rheology: "dry granite" and "mafic granulite" in the upper and lower crust, respectively; **(i-n)** as before for the weak crustal rheology: "dry quartzite" and "wet diorite" in the upper and lower crust, respectively.

WAC and in the western part of the Eucla and Officer basin (Fig. 11i-n). We can further observe that most of Central and Eastern Australia are characterized by fully decoupling conditions, while the lithospheric layers remain fully coupled only in a small part of the WAC and Officer basin, with a consequent significant reduction of the *Te* (Fig. 12 e-f). On the other hand, the strength and *Te* in the off-shore areas seem to be independent on the rheology choice, since the crust is very thin and thus remains in brittle conditions.

In the additional models, we identified the areas, characterized by intermediate thermal conditions, as those more sensitive to the rheology and strain rate variations. Consequently, we should keep in mind that also a temperature uncertainty in the same areas affects the strength and *Te* variations more than in other regions.

6. Conclusions

In this study, we investigated and discussed the thermophysical structure of the Australian continent, which has evolved in time through complex tectonic processes. For this purpose, we constructed a thermal, rheological, and strain rate models, which were employed for calculation of the strength and *Te* variations. The main results are summarized below.

The crustal temperature distribution obtained assuming a steady-state approach, shows thermal anomalies correlated with the surface *HF* variations. The highest temperatures are observed in the NAC, around Tennant Creek, likely on account of the HPEs enrichment, which might extend vertically throughout the crust. The coldest crust underlies the geological provinces east to the WAC, such as the Musgrave Province and the Officer and Eucla basin, indicating more mafic crustal composition. In contrast, the patterns of the temperature variations in the upper mantle, obtained from the joint inversion of seismic velocity and gravity, are more correlated with the age of the tectonic features and less with the heat flow distributions. This can be ascribed to the different depths of the heat sources and length of the heat time diffusion.

The strength distribution in the crust and upper mantle shows different patterns, indicating a strong influence of the temperature variations. The largest values of the integrated crustal strength are observed in the Officer basin and Musgrave Province, while the Yilgarn and Pilbara cratons are characterized by a stiff mantle lithosphere, which retains more than 70% of the total strength. Therefore, these regions are the most tectonically stable areas on a long time scale. In contrast, most of the NAC, SAC, and young Phanerozoic geological provinces retain more than 50% of the strength in the crust and can be affected by crustal and upper mantle flows. The intraplate earthquakes are mostly located in the western part of Australia, where a jump in the integrated crustal strength occurs and along the southeastern margin, in correspondence with the NVP. On the other hand, the NAC is almost aseismic, possibly because the high crustal temperatures yield ductile conditions, preventing earthquakes nucleation.

The *Te* distribution shows that the most rigid area (*Te* > 100 km) corresponds to the western part of Australia, where the lithospheric layers are coupled and the mechanically strong upper mantle layer has a large thickness (M_{mantle} > 50 km). In contrast, low values of *Te* (< 20 km) are found in most of the NAC, the eastern part of the SAC

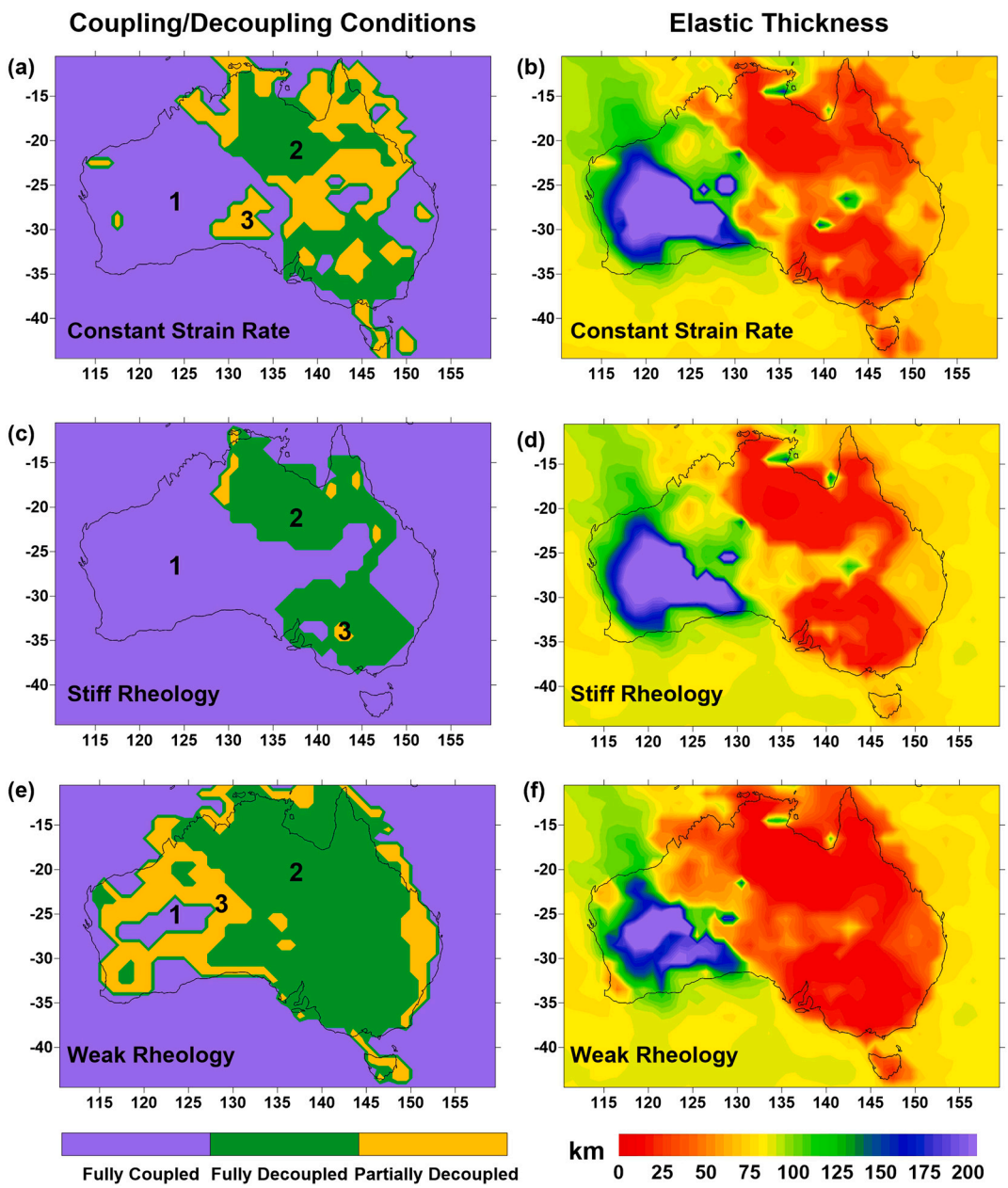

Fig. 12. Coupling/decoupling conditions and effective elastic thickness *Te* (km) for **(a-b)** the fixed amount of strain rate (10^{-15} s^{-1}); **(c-d)** the "stiff" crustal rheology: "dry granite" and "mafic granulite" in the upper and lower crust, respectively; **(e-f)** the "weak" crustal rheology: "dry quartzite" and "wet diorite" in the upper and lower crust, respectively. Black numbers stand as in Fig. 9a.

and in Phanerozoic geological provinces, such as the Lachlan Orogen, where the thickness of the mechanically strong lower crust (M_{lc}) is strongly reduced (< 1 km) and decoupling of the crust from the upper mantle occurs. The crustal rheological model, constructed on the base of the crustal seismic velocity taken from the AuSREM model, emphasizes the influence of temperatures on the strength/*Te* distribution in some regions, such as the Officer basin, and reduces it in some others, such as the Yilgarn craton. The strain rate values, calculated using a global mantle flow model, tend to decrease with the age of the tectonic features and influence the strength/*Te* variations in the opposite way with respect to temperatures.

Declaration of Competing Interest

All the authors read and approved the final manuscript and have no conflict of interest to declare.

Acknowledgements

This study was funded by Trieste University (FABBR-2018), Utrecht University, the Netherlands Research Centre for Integrated Solid Earth Science (ISES-2016-UU-20), and DFG (German Research Foundation) SPP-2017 (PE 2167/2-1).

Appendix A1

We modified the approach of Burov and Diament (1995) and re-estimated *Te* to take into account the Young Modulus's (*E*) depth variations. By definition, the effective elastic plate thickness is the thickness of a homogeneous plate (D_0), whose flexural rigidity is equal to the flexural rigidity of a welded heterogeneous plate (D_1):

$$D_0 = \frac{E_0 T_0^3}{12(1-\sigma_0)} \tag{A1}$$

$$D_1 = \frac{E_1 T_1^3}{12(1-\sigma_1)} \tag{A2}$$

where $E_0 = 100$ GPa is the reference value, E_1 is the Young's Modulus estimated as the Voigt (weighted) average of E of all coupled lithospheric layers (e.g., Altenbach, 2000) Therefore, considering $D_0 = D_1$, we obtain the following:

$$Te_0 = \sqrt[3]{\frac{E_1}{E_0}}\, Te_1 \tag{A3}$$

where Te_1 is the total thickness of the coupled competent layers (A2). In case of decoupling conditions, Te_1 is estimated with the same eq. A3, for each of the decoupled layers (or for two coupled layers and one decoupled) and then equation of Buorov and Diament (1995) can be directly applied with the modified values:

$$T_e^{(n)} = \left(\sum_{i=1}^{n} \Delta h_i^{\,3}\right)^{1/3} \tag{A4}$$

Based on the assumed crustal rheology and on the experimental results of Christensen (1996), we assigned $E = 90$ GPa to the upper crust and values of 99, 106, and 111 GPa to the lower crust, having rheologies of diorite, diabase, and mafic granulite, respectively. We derived the Young's Modulus of the lithospheric mantle by estimating the bulk and shear modulus and the Poisson coefficient of peridotite, its most representative rock, through a mineral physics approach (e.g., Cammarano et al., 2003). We found that the Young's Modulus of the lithospheric mantle is nearly double that of the crustal rocks (180 GPa).

References

Altenbach, H., 2000. An alternative determination of transverse shear stifnesses for sandwich and laminated plates. Int. J. Solids Struct., 37, 3503–3520, doi:10.1016/S00207683(99)00057-8.

Burov, E.B., M. Diament, 1995. The effective elastic thickness of (Te) continental lithosphere. What does it really means?. J. Geophys. Res., 100(B3), 3905–3927, doi:10.1029/ 94JB02770.

Cammarano, F., S. Goes, P. Vacher, and D. Giardini, 2003. Inferring upper-mantle temperatures from seismic velocities. Phys. Earth Planet. Inter., 138, 197–222 doi:10.1016/S00319201(03)00156-0.

Christensen, N.I., 1996. Poisson's ratio and crustal seismology. J. Geophys. Res., 101(B2),3139–3156,doi:10.1029/95JB03446.

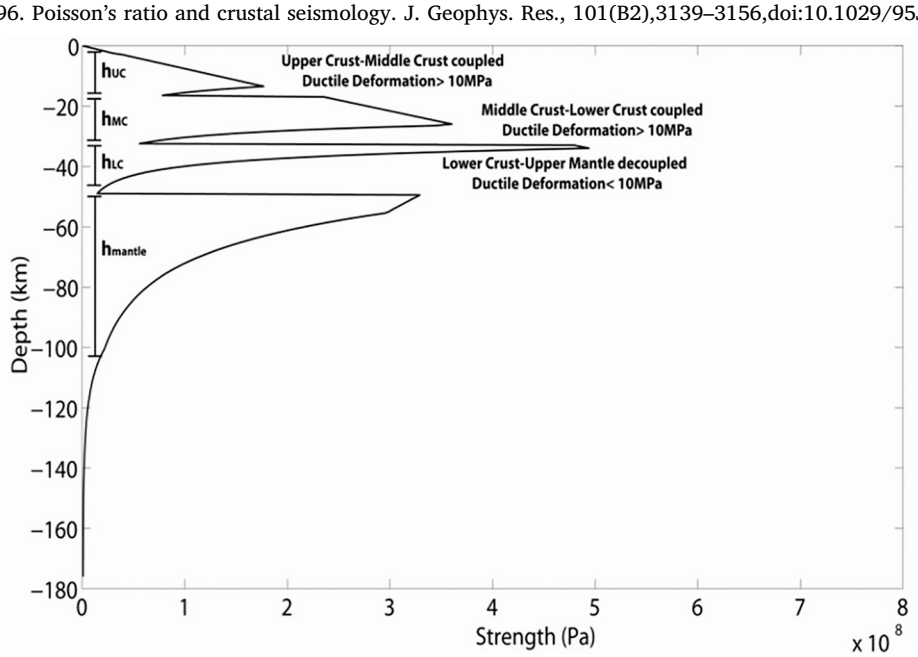

Fig. A1. Example of a strength profile, showing the thickness of each mechanically strong lithospheric layer, for a crustal subdivision in three layers, and how coupling and decoupling conditions are obtained.

References

Afonso, J.C., Fullea, J., Yang, Y., Connolly, J.A.D., Jones, A.G., 2013. 3-D multi-observable probabilistic inversion for the compositional and thermal structure of the lithosphere and upper mantle. II: General methodology and resolution analysis. J. Geophys. Res. 118 (4), 1650–1676. https://doi.org/10.1002/jgrb.50123.

Aitken, A.R.A., Altinay, C., Gross, L., 2015. Australia's lithospheric density field, and its isostatic equilibration. Geophys. J. Int. 203, 1961–1976.

Aitken, A.R.A., Betts, P.G., Young, D.A., Blankenship, D.D., Roberts, J.L., Siegert, M.J., 2016. The Australo-Antarctic Columbia to Gondwana transition. Gondwana Res. 29, 136–152.

Argus, D.F., Gordon, R.G., DeMets, C., 2011. Geologically current motion of 56 plates relative to the no-net-rotation reference frame. Geochem. Geophys. Geosyst. (G3) 12 (11), Q11001. https://doi.org/10.1029/2011GC003751.

Békési, E., Lenkey, L., Limberger, J., Porkoláb, K., Balázs, A., Bonté, D., Vrijlandtd, M., Horváth, F., Cloetingh, S., van Wees, J.-D., 2018. Subsurface temperature model of the Hungarian part of the Pannonian Basin. Glob. Planet. Chang. 171, 48–64. https://doi.org/10.1016/j.gloplacha.2017.09.020.

Betts, P.G., Armit, R.J., Stewart, J., Aitken, A.R.A., Ailleres, L., Donchak, P., Hutton, L., Withnall, I., Giles, D., 2016. Australia and Nuna. Geol. Soc. Spec. Publ. 47–81.

Bürgmann, R., Dresen, G., 2008. Rheology of the lower crust and upper mantle: evidence from rock mechanics, geodesy and field observations. Annu. Rev. Earth Planet. Sci. 36, 531–561.

Burov, E.B., 2011. Rheology and strength of the lithosphere. Mar. Pet. Geol. 28, 1402–1443. https://doi.org/10.1016/j.marpetgeo.2011.05.008.

Burov, E.B., Diament, M., 1995. The effective elastic thickness (*Te*) of continental lithosphere. What does it really means? J. Geophys.Res. 100, 3895–3904.

Byerlee, J.D., 1978. Friction of rocks. Pure Appl. Geophys. 116, 615–626.

Carter, N.L., Tsenn, M.C., 1987. Flow properties of continental lithosphere. Tectonophysics 136, 27.

Čermák, V., Bodri, L., Rybach, L., Buntebarth, G., 1990. Relationship between seismic velocity and heat production: Comparison of two sets of data and test of validity. Earth Planet. Sci. Lett. 99, 48–57.

Chapman, D.S., 1986. Thermal gradients in the continental crust. From Dawson et al. (eds.), 1986, the Nature of the lower Continental Crust. Geol. Soc. Spec. Publ. 24, 63–70.

Chopping, R., Kennett, B.L.N., 2015. Maximum depth of magnetisation of Australia, its uncertainty, and implications for Curie depth. GeoResJ 7, 70–77.

Christensen, N.I., Mooney, W.D., 1995. Seismic velocity structure and composition of the continental crust: a global review. J. Geophys. Res. 100 (B6), 9761–9788.

Clitheroe, G.M., Gudmundsson, O., Kennett, B.L.N., 2000. The crustal thickness of Australia. J. Geophys. Res. 105, 13697–13713.

Craig, T.J., Jackson, J.A., Priestley, K., McKenzie, D., 2011. Earthquake distribution patterns in Africa: their relationship to variations in lithospheric and geological structure, and their rheological implications. Geophys. J. Int. 185, 403–434.

Cull, J.P., 1982. An appraisal of Australian heat-flow data. J. oAustralian Geol. Geophysics 7, 11–21.

Cull, J.P., 1991. Heat flow and regional geophysics in Australia. In: Terrestrial Heat Flow and the Lithosphere Structure, eds. V. Cermak and L. Rybach, pp. 486–500. Springer-Verlag, Berlin.

Cull, J.P., Conley, D., 1983. Geothermal gradients and heat flow in Australian sedimentary basins. J. Australian Geol. Geophysics 8, 32–337.

Demouchy, S., Tommasi, A., Boffa-Ballaran, T., Cordier, P., 2013. Low strength of Earth's uppermost mantle inferred from tri-axial deformation experiments on dry olivine crystals. Phys. Earth Planet. Inter. 220, 37–49.

Fichtner, A., Kennett, B.L.N., Igel, H., Bunge, H.P., 2010. Full waveform tomography for radially anisotropic structure: New insights into present and past states of the Australasian upper mantle. Earth Planet. Sci. Lett. 290, 270–280.

Fishwick, S., Rawlinson, N., 2012. 3-D structure of the Australian lithosphere from evolving seismic datasets. Australian Journal of Earth Sciences: An International Geoscience Journal of the Geological Society of Australia 59 (6), 809–826.

Fishwick, S., Reading, A.M., 2008. Anomalous lithosphere beneath the Proterozoic of western and Central Australia: a record of continental collision and intraplate deformation? Precambrian Res. 166, 111–121.

François, T., Burov, E.B., Meyer, B., Agard, P., 2013. Surface topography as key constraint on thermo-rheological structure of stable cratons. Tectonophysics 602, 106–123.

Goes, S., Simons, F.J., Yoshizawa, K., 2005. Seismic constraints on temperature of the Australian uppermost mantle. Earth Planet. Sci. Lett. 236, 227–237.

Goetze, C., Evans, B., 1979. Stress and temperature in the bending lithosphere as constrained by experimental rock mechanics. Geophys. J. R. Astron. Soc. 59, 463–478.

Goutorbe, B., Lucazeau, F., Bonneville, A., 2008. Surface heat flow and the mantle contribution on the margins of Australia. Geochem. Geophys. Geosyst. https://doi.org/10.1029/2007GC001924. (G3) 9, Q05011.

Hasterock, D., Chapman, D.S., 2011. Heat production and geotherms for the continental lithosphere. Earth Planet. Sci. Lett. 307, 59–70.

Hasterock, D., Gard, M., 2016. Utilizing thermal isostasy to estimate sub-lithospheric heat flow and anomalous crustal radioactivity. Earth Planet. Sci. Lett. 450, 197–207.

Hasterock, D., Webb, J., 2017. On the radiogenic heat production of igneous rocks. Geosci. Front. 8, 919–940.

Haynes, M.W., Budd, A.R., Gerner, E.J., Harris-Pascal, C., Kirkby, A.L., 2015. TherMAP – Assessing Subsurface Temperatures in Australia from a Geothermal Systems Perspective. In: Proceedings World Geothermal Congress 2015, Melbourne, Australia, 19–25 April 2015.

Jackson, J., 2002. Strength of the continental lithosphere: time to abandon the jelly sandwich? GSA Today 12 (9), 4–9.

Kaban, M.K., Petrunin, A.G., Schmeling, H., Shahraki, M., 2014. Effect of decouplingof lithospheric plates on the observed geoid. Surv. Geophys. 35, 1361–1373. https://doi.org/10.1007/s10712-014-9281-3.

Kennett, B.L.N., Salmon, M., 2012. AuSREM: Australian Seismological Reference Model. Aust. J. Earth Sci. 59, 1091–1103.

Kennett, B.L.N., Fichtner, A., Fishwick, S., Yoshizawa, K., 2013. Australian seismological referencemodel (AuSREM): Mantle component. Geophys. J. Int. 192, 871–887.

Lee, C.-T.A., 2003. Compositional variation of density and seismic velocities in natural peridotites at STP conditions: Implications for seismic imaging of compositional heterogeneities in the upper mantle. J. Geophys. Res. 108, 2441. https://doi.org/10.1029/2003JB002413. (B9.

Lucazeau, F., 2019. Analysis and Mapping of an Updated Terrestrial Heat Flow Data Set. Geochem. Geophys. Geosyst. (G3) 20, 4001–4024. https://doi.org/10.1029/2019GC008389.

Mather, B., McLaren, S., Taylor, D., Roy, S., Moresi, L., 2018. Variations and controls on crustal thermal regimes in Southeastern Australia. Tectonophysics 723 (16), 261–276.

Matthews, C., Beardsmore, G., 2007. New heat flow data from south-Eastern South Australia. Explor. Geophys. 38, 260–269.

Matthews, C., Beardsmore, G., Driscoll, J., Pollington, N., 2013. Heat flow data from the southeast of South Australia: distribution and implications for the relationship between current heat flow and the Newer Volcanics Province. Explor. Geophys. 44 (2), 133–144.

Mazzotti, S., 2007. Geodynamic models for earthquake studies in intraplate North America, in Continental Intraplate Earthquakes: Science, Hazard, and Policy Issues. Geol. Soc. Am. Spec. Pap. 425. edited by S. Stein and S. Mazzotti. pp. 17–33. https://doi.org/10.1130/2007.2425(02).

McLaren, S., Dunlap, W.J., Sandiford, M., McDougall, I., 2002. Thermochronology of high heat-producing crust at mount painter, South Australia: Implications for tectonic reactivation of continental interiors. Tectonics 21 (4), TC001275. https://doi.org/10.1029/2000tc001275.

McLaren, S., Sandiford, M., Hand, M., Neumann, N., Wyborn, L., Bastrakova, I., 2003. The hot southern continent: heat flow and heat production in Australian Proterozoic terranes. Geological Society of Australia Special Publication 22, 151–161.

Middleton, M., 2016. Radiogenic Heat Generation in Western Australia —Implications for Geothermal Energy. https://doi.org/10.5772/61963.

Mooney, W.D., Ritsema, J., Hwang, Y.K., 2012. Crustal seismicity and the earthquake catalog maximum moment magnitude (Mcmax) instable continental regions (SCRs): Correlation with the seismic velocity of the lithosphere. Earth Planet. Sci. Lett. 357–358, 78–83.

Petrunin, A.G., Kaban, M.K., Rogozhina, I., Trubitsyn, V., 2013. Revising the spectral method as applied to modeling mantle dynamics. Geochem. Geophys.Geosyst. (G3) 14 (9), 3691–3702.

Pollett, A., Raimondo, T., Halpin, J.A., Hand, M., Bendall, B., McLaren, S., 2019. Heat flow in soutern Australia and connections with East Antarctica. Geochem. Geophys. Geosyst. (G3) 20, 5352–5370. https://doi.org/10.1029/2019GC008418.

Raimondo, T., Hand, M., Collins, W.J., 2014. Compressional intracontinental Orogens: Ancient and modern perspectives. Earth Sci. Rev. 130, 128–153.

Ranalli, G., 1994. Nonlinear flexure and equivalent mechanical thickness of the lithosphere. Tectonophysics 240 (1), 107–114.

Rawlinson, N., Salmon, M., Kennett, B.L.N., 2014. Transportable seismic array tomography in Southeast Australia: Illuminating the transition from Proterozoic to Phanerozoic lithosphere. Lithos 189, 65–76.

Rybach, L., Buntebarth, G., 1984. The variation of heat generation, density and seismic velocity with rock type in the continental lithosphere. Tectonophysics 103, 335–344.

Salmon, M., Kennett, B.L.N., Saygin, E., 2013. Australian seismological referencemodel (AuSREM): Crustal component. Geophys. J. Int. 192, 190–206.

Sandiford, M., Hand, M., McLaren, S., 2001. Tectonic feedback, intraplate orogeny and the geochemical structure of the crust: a central Australian perspective. Special Publication – Geological Society of London 184, 195–218.

Sandiford, M., Mclaren, S., Neumann, N., 2002. Long-term thermal consequences of the redistribution of heat-producing elements associated with large-scale granitic complexes. J. Metamorph. Geol. 20, 87–98. https://doi.org/10.1046/j.0263-4929.2001.00359.x.

Siégel, C., Schrank, C.E., Bryan, S.E., Beardsmore, G.R., Purdy, D.J., 2014. Heat-producing crust regulation of subsurface temperatures: a stochastic model re-evaluation of the geothermal potential in southwestern Queensland, Australia. Geothermics 51, 182–200.

Sloan, R.A., Jackson, J.A., McKenzie, D., Priestley, K., 2011. Earthquake depth distributions in Central Asia, and their relations with lithosphere thickness, shortening and extension. Geophys. J. Int. 185, 1–29.

Stixrude, L.C. Lithgow-Bertelloni, 2005. Thermodynamics of mantle minerals—I. Physical properties. Geophys. J. Int. 162, 610–632.

Swain, C.J., Kirby, J.F., 2006. An effective elastic thickness map of Australia from wavelet transforms of gravity and topography using Forsyth's method. Geophys. Res. Lett. 33, L02314. https://doi.org/10.1029/2005GL025090.

Tesauro, M., Kaban, M.K., Cloetingh, S.A.P.L., 2008. EuCRUST-07: a new reference model for the European crust. Geophys. Res. Lett. 35, L05313.

Tesauro, M., Burov Kaban, M.K., Cloetingh, S.A.P.L., 2011. Ductile crustal flow in Europe's lithosphere. Earth Planet. Sci. Lett. 312, 254–265.

Tesauro, M., Audet, P., Kaban, M.K., Bürgmann, R., Cloetingh, S.A.P.L., 2012. The effective elastic thickness of the continental lithosphere:Comparison between rheological and inverse approaches. Geochem. Geophys. Geosyst. https://doi.org/10.1029/2012GC004162. (G3) 13, 9, Q09001.

Tesauro, M., Kaban, M.K., Mooney, W.D., Cloetingh, S.A.P.L., 2014. NACr14: A 3D model for the crustal structure of the North American Continent. Tectonophysics 631,

65–86.
Tesauro, M., Kaban, M.K., Mooney, W.D., 2015. Variations of the lithospheric strength and elastic thickness in North America. Geochem. Geophys. Geosyst. https://doi.org/10.1002/2015GC005937. (G3) 16.
Tesauro, M., Kaban, M.K., Aitken, A.R.A., 2020. Thermal and compositional anomalies of the Australian upper mantle from seismic and gravity data. Geochem. Geophys. Geosyst (G3) (under review).
Watts, A.B., Burov, E., 2003. Lithospheric strength and its relationship to the elastic and seismogenic layer thickness. Earth Planet. Sci. Lett. 213, 113–131.
Wilks, K.R., Carter, N.L., 1990. Rheology of some continental lower crustal rocks. Tectonophysics 182, 57–77.
Williams, H.A., Betts, P.G., 2009. The Benagerie Shear Zone: 1100 Myr of reactivation history and control over continental lithospheric deformation. Gondwana Res. 15, 1–13.
Zhao, J., McCulloch, M.T., Korsch, R.T., 1994. Characterisation of a plume-related approximately 800 Ma magmatic event and its implications for basin formation in Central-Southern Australia. Earth Planet. Sci. Lett. 121, 349–367.
Zuber, M.T., Betchel, T.D., Forsith, D.W., 1989. Effective elastic thicknesses of the lithosphere and mechanisms of isostatic compensation in Australia. J. Geophys. Res. 94, 9353–9367.